A gaseous detector for ultracold neutrons in the n2EDM project Student

William D Saenz Arevalo, Francesco Recchia, Thomas Lefort

▶ To cite this version:

William D Saenz Arevalo, Francesco Recchia, Thomas Lefort. A gaseous detector for ultracold neutrons in the n2EDM project Student. [University works] Universite de Caen Normandie. 2019, pp.1-61. in2p3-02957354

HAL Id: in2p3-02957354
https://hal.in2p3.fr/in2p3-02957354

Submitted on 5 Oct 2020

UNIVERSITÀ
DEGLI STUDI
DI PADOVA

lpc caen
Laboratoire de physique corpusculaire

Erasmus Mundus
JMD on
Nuclear Physics

EMJMD ON EXPERIMENTAL NUCLEAR PHYSICS

MASTER THESIS

A gaseous detector for ultracold neutrons in the n2EDM project

Student:
William D. Saenz Arevalo

Supervisors:
Francesco Recchia
Thomas Lefort

2018/2019

Contents

Abstract

The experimental arrangement of the n2EDM project, which aims at the measurement of the neutron electric dipole moment (d_n), is in its construction phase. Currently, it is being evaluated for possible improvements that would lead to a greater ultra-cold neutron (UCN) counting efficiency and a larger sensitivity on the determination of d_n. This work introduces a novel gaseous detector, which functioning is based on the absorption reaction n + ^{3}He → ^{1}H + ^{3}H followed by the CF_4 scintillation process. The counting capabilities for this detector are studied at two facilities that produce UCN from different mechanisms, one from spallation processes at the Paul Scherrer Institute (PSI), and the other from uranium fission at the TRIGA nuclear reactor in Mainz. Determination of parameters that optimize the UCN detection was also achieved, in particular, the gas pressure: 25 mbar for ^{3}He and 400 mbar for CF_4. Pulse shape discrimination techniques allowed the background events identification, estimated in a 2% of the total counts at PSI. The absolute comparison against a cascade detector shows that the new prototype is doubly more efficient, that converts it in one of the most suitable alternatives for the UCN counting in the upcoming n2EDM experiment.

Resumen

El arreglo experimental del proyecto n2EDM, que busca medir el momento dipolar eléctrico del neutrón (d_n), está en su fase de construcción. Actualmente se evalúan las posibles mejoras que impliquen una mayor eficiencia en el conteo de neutrones ultra fríos (UCN) y una sensibilidad superior en la determinación de d_n. Este trabajo presenta un nuevo detector gaseoso, cuyo funcionamiento se basa en la reacción de absorción n + ^{3}He → ^{1}H + ^{3}H y el posterior proceso de centelleo en CF_4. La capacidad de conteo de este detector se estudia en dos laboratorios que producen UCN desde distintas fuentes, uno a partir de procesos de espalación en el Instituto Paul Scherrer (PSI), y el otro desde la fisión de uranio en el reactor nuclear TRIGA en Mainz. También se lograron establecer parámetros que optimizan la detectión de UCN, en particular la presión de los gases: ^{3}He a 25 mbar y CF_4 a 400 mbar. Técnicas de discriminación de pulsos permitieron la identificación de eventos de radiación fondo, que fueron estimados en un 2 % del total de las cuentas en PSI. La comparación directa contra el desempeño de un detector de cascada muestra que el nuevo prototipo es dos veces más eficiente, convirtiendolo en una de las mejores alternativas para el conteo de UCN en el futuro experimento n2EDM.

1 Introduction

Measuring the electric dipolar moment (EDM) of particles, atoms, or even molecules represents a means to test fundamental symmetries in physics [1]. While current theoretical models, such as the standard model (SM), can explain some of the observed violated symmetries, various others have been modified or even rejected due to their lack of prediction. Therefore, EDM experiments are regarded as validation probes for fundamental models of particle physics.

Currently, several experiments around the world are being planned with the purpose of showing evidence of permanent EDMs. In the past, not even one has succeeded in such labor. All the conclusions have been -*if it exists, it should be smaller than*-. This conclusion reflects two facts; first, EDMs might be amazingly tiny, and second, these measurements became technically extremely challenging. Nevertheless, no one knows today if the next attempts will finally result in -*its magnitude is*-.

In the search of new physics, the neutron appears as one of the most promising probes. In fact, the first experiment of the EDM-kind was focused on this fermion[2]. Since then, around 15 distinct experiments have intended the measurement of the neutron EDM. In this long process, techniques have evolved to the point that most of the future projects are proposed with ultra-cold neutrons (UCN) as the subject of study. Consequently, new challenges emerge in matters of high intense UCN sources, adequate UCN transport, reliable UCN storage systems, and efficient UCN detectors.

A brief description of the neutron EDM study, the n2EDM project, and some of the available UCN sources and detectors are presented in the rest of this introduction. In section 2 a novel UCN gaseous detector is exposed. Details of its working principle, acquisition system, and main components are mentioned. Then, in sections 3 and 4, the performance of this new prototype is reported at two different UCN facilities. Finally, in section 5, conclusions and perspectives of the novel detector in the future n2EDM experiment are discussed.

1.1 Neutron electric dipole moment

In quantum mechanics, measuring a nonzero EDM of a system in its ground state is regarded as a proof of symmetries violation. To see this, one can start from the Hamiltonian associated to a particle with electric ($\vec{d}$) and magnetic ($\vec{\mu}$) dipole moments, immerse in an electric $\vec{E}$ and a magnetic $\vec{B}$ fields:

$$\hat{\mathcal{H}} = -\vec{\mu}\cdot\vec{B} - \vec{d}\cdot\vec{E}. \tag{1}$$

The effect of $\mathcal{P}$ and $\mathcal{T}$ transformations on this system is straightforward if looking at the influence on the individual observables, which are summarized in Table 1. It comes to the view that

$$\mathcal{P}\{\hat{\mathcal{H}}\} = -\vec{\mu}\cdot\vec{B} + \vec{d}\cdot\vec{E} \neq \pm\hat{\mathcal{H}}, \tag{2}$$
$$\mathcal{T}\{\hat{\mathcal{H}}\} = -\vec{\mu}\cdot\vec{B} + \vec{d}\cdot\vec{E} \neq \pm\hat{\mathcal{H}}, \tag{3}$$

demonstrating $\mathcal{P}$, $\mathcal{T}$ and $\mathcal{CP}$ (under the $\mathcal{CPT}$ theorem [3]) symmetries violation. In particular, it would be of great interest finding this new source of $\mathcal{CP}$-violation since it would explain the baryogenesis imbalance, while revealing the need to formulate physics beyond the SM*[4].

Table 1 – Effect of $\mathcal{C}$, $\mathcal{P}$ and $\mathcal{T}$ transformations on the observables described by a particle with electric and magnetic dipole moments.

observable	$\mathcal{C}$	$\mathcal{P}$	$\mathcal{T}$
Magnetic dipole moment $\vec{\mu}$	$\vec{\mu}$	$\vec{\mu}$	$-\vec{\mu}$
Electric dipole moment $\vec{d}$	$\vec{d}$	$\vec{d}$	$-\vec{d}$
Magnetic field $\vec{B}$	$-\vec{B}$	$\vec{B}$	$-\vec{B}$
Electric field $\vec{E}$	$-\vec{E}$	$-\vec{E}$	$\vec{E}$

Since 1957, the neutron has been chosen among quantum systems in repeated occasions to perform EDM measurements. Working with this spin-1/2 fermion brings some practical advantages. First, its zero net charge enables the use of electric fields without altering the dynamics. Also, the absence of quadrupole and higher electromagnetic (EM) moments† implies purely dipolar behavior when electric and magnetic fields are implemented. As will be noted later, both of these fields are necessary for neutron EDM measurements.

---

[*] Currently, the SM explains $\mathcal{CP}$-violation in the electroweak sector, but it cannot account for the baryon asymmetry of the universe.

[†] As a result of the Wigner-Eckart theorem, a system with spin S can have EM moments of order up to $2S+1$. Thus, for the neutron up to 2 (dipole moments).

Forty-nine years passed from the first (Smith, Purcell and Ramsey [2]) to the last (Baker *et al* [5]) publication reporting on the neutron EDM. Through these decades, experimental results have decreased the upper limit of d_n, reaching the current limit 2.9×10^{-26} e cm (90% C.L.). The neutron EDM, if existing, should have a magnitude smaller than this value. Figure 1 depicts the evolution in time of the upper bound established by different experiments. It is observed that, after 1980, UCN were preferred over other techniques employing the neutron-beam magnetic resonance.

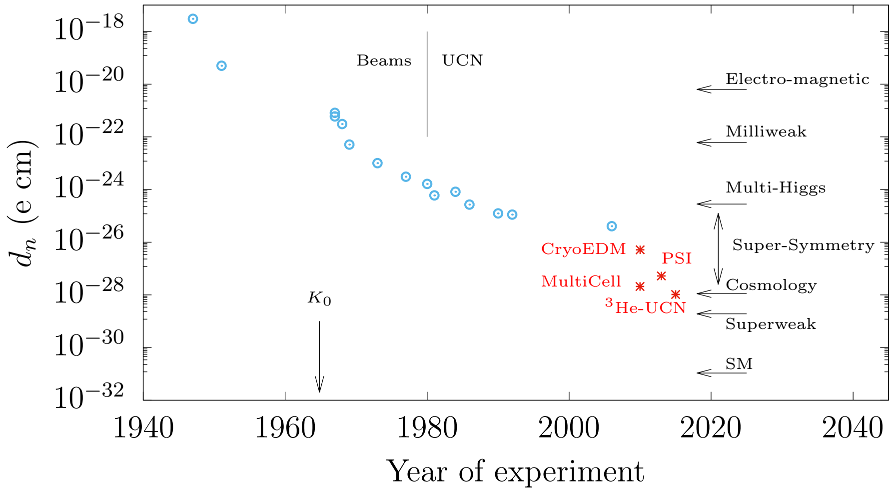

Figure 1 – Drop of the d_n upper bound in time. Blue circles correspond to already published results while red asterisks to predictions of upcoming projects. The last reported value by the RAL-Sussex-ILL collaboration [5] took place in 2006. On the right side, nEDM ranges predicted from various theoretical models are displayed. K_0 represents the date at which the $\mathcal{CP}$-noninvariance in the decay of the neutral kaon was evidenced. Figure adapted from [6].

The shortening of the d_n upper limit has been possible thanks to the experimental techniques improvements along the years. As will be noted in the following section, the quality of an EDM measurement relies on the capacity to separate spurious electric and magnetic fields that could induce a false EDM signal. One of the main changes implemented in the pursuit of reducing the systematic effects was the use of UCN instead of neutron beams. In the latter, the so-called $\vec{E} \times \vec{v}$ effect, that emerges from the relative motion of neutron with respect to electric fields, produces a significant systematic effect due to the large neutron velocities (in contrast to the UCN).

1.2 The n2EDM project

n2EDM is the second phase of the *nEDM* project. Its aim is to reduce the d_n upper limit by one order of magnitude [7], i.e., at the level of 10^{-27} e cm. Although the method proposed to determine the magnitude of d_n, namely the *separated oscillatory fields method* (Ramsey [8]), is still the same, several features of the approach have been improved so to achieve the refinement in the experimental sensitivity [9]. In the following, a brief description of the working principle behind the nEDM measurement and the Ramsey's method are presented.

1.2.1 Experimental approach

The proposed technique exploits the magnetic resonance phenomenon and evaluates the effects that an eventual intrinsic EDM would have on the Larmor frequency of the system. It is well known that particles with permanent magnetic dipole moments (MDM) experience a precession motion in the presence of static magnetic fields, whose frequency is proportional to the scalar product of the magnetic moment $\vec{\mu}$ and the external field $\vec{B}$. Similarly, particles with permanent EDM ($\vec{d}$) would precess in the presence of static electric field ($\vec{E}$). In order to describe a system with both MDM and EDM, the Hamiltonian of equation 1 is rewritten as

$$\hat{\mathcal{H}} = -\vec{\mu} \cdot \vec{B} - \vec{d} \cdot \vec{E} = -(\mu\vec{B} + d\vec{E}) \cdot \frac{\vec{S}}{|\vec{S}|}. \tag{4}$$

In this expression, it has been assumed that $\vec{\mu}$ and $\vec{d}$ are parallel to the spin $\vec{S}$. Thus, for the neutron ($S = 1/2$):

$$\hat{\mathcal{H}} = -2(\mu_n\vec{B} + d_n\vec{E}) \cdot \vec{S}. \tag{5}$$

Experimentally, this equation has two versions, one for parallel and the other for anti-parallel fields. Figure 2 shows the energy levels observed in both cases. It results that the energy separation (ΔE) between spin-up and spin-down configurations is larger when the fields are parallel:

$$\Delta E_{\parallel} = h\nu_{\parallel} = 2(\mu_n B + d_n E), \qquad \Delta E_{\nparallel} = h\nu_{\nparallel} = 2(\mu_n B - d_n E), \tag{6}$$

here ν denotes the precession frequency. This difference between the parallel and anti-parallel configurations is the keystone of all the EDM experiments involving magnetic resonances. If the frequencies associated to both cases are determined, the magnitude of the dipole is directly calculated as

$$d_n = \frac{h(\nu_{\parallel} - \nu_{\nparallel})}{4E}. \tag{7}$$

Therefore, the nEDM measurement is reduced to the determination of the frequency shift $\delta\nu = \nu_{\parallel} - \nu_{\nparallel}$, which is in the order of 0.1 μHz for electric fields of around 10 kV/cm and assuming a d_n of 10^{-26} e cm. The Ramsey method, regarded as the most efficient method to measure precession frequencies is used for this purpose.

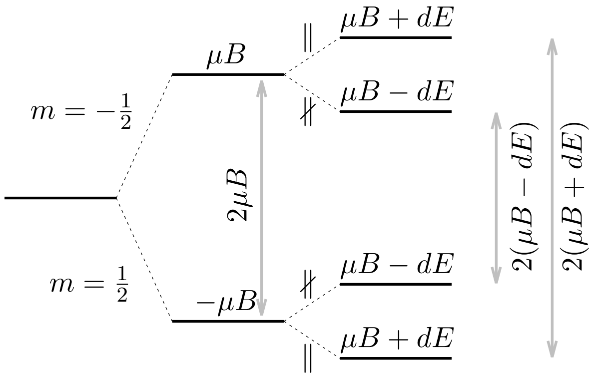

Figure 2 – Splitting of energy levels in parallel and anti-parallel configurations. Left side corresponds to no fields, the intermediate region to a single magnetic field and the right side to both electric and magnetic fields. It is assumed here that $\vec{\mu}$ and $\vec{d}$ are oriented along $\vec{S}$ in the same way.

1.2.2 Ramsey's method of separated oscillatory fields

The Ramsey's method is an improved version of Rabi's method [10]. In both cases, an oscillatory magnetic field $\vec{B}_{\text{osc}}$, perpendicular to the static $\vec{E}$ and $\vec{B}$ fields, induces the transition between the spin-up and spin-down states. The transition probability reaches a maximum value when the magnetic field frequency (ν_{osc}) matches the Larmor frequency. In the resonance configuration, the spin flip occurs at the Rabi's frequency ν_R, meaning that after a period $t = (2\nu_R)^{-1}$ all the spins experience a complete inversion. Such effect is known as a "π-pulse" inversion.

The main difference between Rabi's and Ramsey's schemes is the approach followed to achieve the spin inversion. Assuming a set of spin-up $(+\hat{z})$ systems, Rabi's method uses a π-pulse to invert and populate the spin-down states $(-\hat{z})$. Ramsey instead proposes an intermediate -free precession- stage. During the first part, a $\pi/2$-pulse induces half inversion only; it can be thought of as rotating the spins from the $+\hat{z}$ axis to the $\hat{x}$-$\hat{y}$ plane. Once there, the systems are allowed to freely evolve ($\vec{B}_{\text{osc}}$ is turned off) during a time $t_{\text{free}} \gg t_{\upharpoonleft\downharpoonright}$, and then, a second $\pi/2$-pulse completes the inversion. It is crucial for this process that both $\pi/2$-pulses are in phase so to guarantee the expected total inversion ("π-pulse" effect). Figure 3 describes the three steps involved in Ramsey's method.

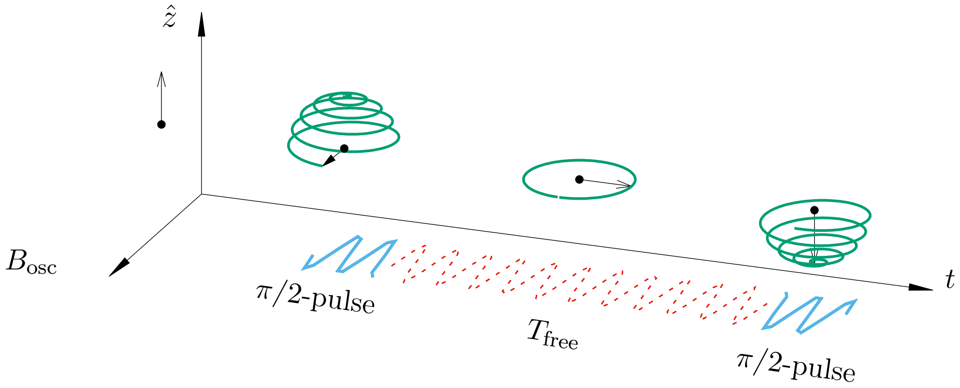

Figure 3 – Description of the different stages in Ramsey's method. An oriented spin $(+\hat{z})$ is inverted after two coherent $\pi/2$-pulses separated by a free precession period (T_{free}). During this intermediate time, the oscillatory field is turned off thus allowing the spin to precess on the $\hat{x}$-$\hat{y}$ plane.

The power of Ramsey's technique comes with the free oscillation stage. During that time, an overall phase proportional to T_{free} characterizes the spin state that precess on the $\hat{x}$-$\hat{y}$ plane. Only when the second pulse is coherent with the first one, the inversion is perfectly completed. On the other hand, if at the end of the free oscillation period there exist a small difference between the frequencies ν_{osc} and $\nu_{\nparallel,\parallel}$, the spin state will have gained a relative phase $2\pi(\nu_{\text{osc}} - \nu_{\nparallel,\parallel})t_{\text{free}}$ with respect to the second pulse. Then, the inversion probability is hindered and only a fraction of the spins will be inverted.

When this three-stages process is run for several ν_{osc}, the number of systems achieving the total inversion describes an oscillatory pattern whose maxima correspond to the resonance frequencies $\nu_{\text{osc}} = \nu_{\nparallel,\parallel}$ (and its integer multiples). The advantages of Ramsey's technique are reflected in the resonance linewidth

(Γ_R) associated to this oscillatory pattern. It represents 0.6 of those achieved by other conventional approaches, such as Rabi's method [8]. This benefit has a direct influence on the power to resolve the magnitude of $\nu_{\parallel}$ and $\nu_{\nparallel}$. At the same time, since Γ_R is inversely proportional to T_{free}, the undesired systematic effects present in the free-precession stage can be largely reduced.

1.2.3 Experimental setup and nEDM measuring

A general description of the experimental proposal is displayed in Figure 4. UCN coming from the source pass through a polarizer superconducting magnet (1) so to prepare the spins in an oriented state. Then, a switch (2) guides the UCN to the storage chamber (3) in where the three stages of Ramsey's method take place. The chamber and its container are vacuumed with turbopumps (4), which lie just outside the magnetic shielding walls (5). They are supported by an aluminum base and four granite pillars (6). When the resonance cycle is finished, the precession chamber is emptied and UCN polarization is analyzed in the detection system (7). The whole setup is surrounded by an insulating and thermalized shell (8) that also compensates magnetic perturbations produced by the environment. One of the main improvements of the current apparatus is found in the storage chamber. It is made of two precession chamber, one with $E \parallel B$ and the other with $E \nparallel B$. This simultaneous configuration avoids systematic effects generated by the inversion of the electric field.

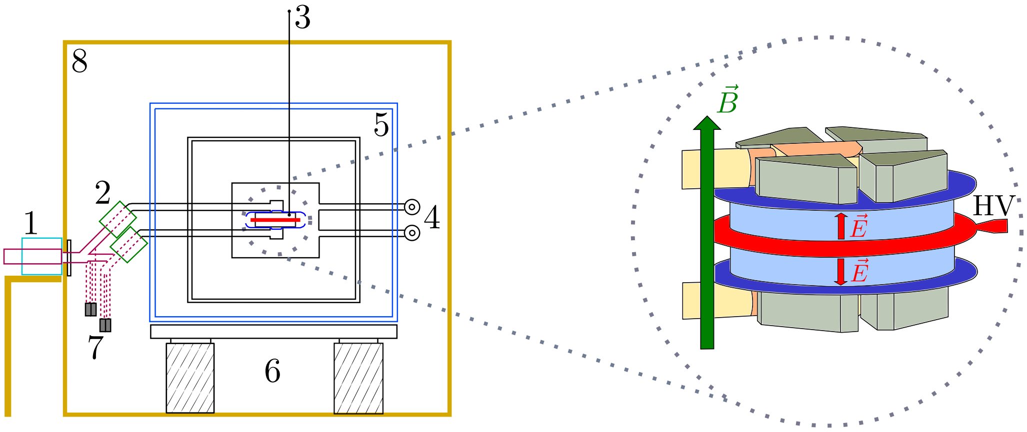

Figure 4 – Main components in the n2EDM project setup. The explanation of the labels is found in the text. On the right side a zoom of the precession chamber showing the electric and magnetic fields directions. Figure adapted from [7].

At the end of Ramsey's cycle and depending on the field frequency ν_{osc}, a certain fraction of the UCN will be detected with positive ($N_{\uparrow}$) and negative ($N_{\downarrow}$) spins [‡]. In resonance configuration and assuming that all spins start with positive polarization, $N_{\downarrow}$ and $N_{\uparrow}$ are expected to reach the maximum N_{max} and minimum N_{min} values, respectively. A spin analyzer, located between the switch and detectors (2 and 7 in Figure 4), transmits one polarized-state only and carries out the $N_{\uparrow}$ and $N_{\downarrow}$ counting.

After working out the Ramsey's equation that accounts for the transition probability from spin-up to spin-down states, the fraction of UCN detected in either case is given by [1]

$$N_{\uparrow\downarrow}(\Delta\nu) = \frac{N_0}{2}\left(1 \mp \alpha\cos(2\pi[\nu_{\text{osc}} - \nu_{\nparallel,\parallel}]T_{\text{free}})\right) \tag{8}$$

in where ↑ and ↓ correspond to $-$ and $+$, respectively, and α is a constant representing the polarization level achieved at the end of the measurement, defined as

$$\alpha \equiv \frac{N_{\text{max}} - N_{\text{min}}}{N_{\text{max}} + N_{\text{min}}}. \tag{9}$$

Once the frequencies $\nu_{\parallel}$ and $\nu_{\nparallel}$ are calculated from fitting equations 8 to the data, the nEDM evaluation is straightforward with equation 7. The uncertainty σ_{d_n} in that case is expressed as

$$\sigma_{d_n} = \frac{\hbar}{2\alpha E T_{\text{free}}\sqrt{N_0}} \tag{10}$$

1.3 Production of UCN

The n2EDM experiment is to be performed with the UCN source at the Paul Scherrer Institute (PSI). The large UCN density produced at this facility ensures a high UCN delivery flux, which is appropriated to decrease the uncertainty of σ_{d_n} (see equation 8). There are around a dozen facilities in the world intended to provide UCN for different purposes, some of them specially designed for nEDM experiments [11, 12, 13, 14, 15].

Just as it happens with all the energy ranges used to classify neutrons, UCN energies do not have a precise limiting value. Instead, neutrons are referred to as UCN in virtue of their interaction mechanism, which in turn

---

[‡] The total amount of UCN is denoted as $N_0 = N_{\uparrow} + N_{\downarrow}$.

defines their macroscopic behavior. Roughly speaking, when neutrons reach energies below the Fermi potential for a given material, they experience total reflection after impinging on a surface made out of that material [16]. Indeed, reflection occurs if the normal component of the neutron velocity v_n is smaller than the Fermi velocity v_F (see Figure 5). As a consequence of that phenomenon, neutrons can be easily stored in closed containers and transported through guide tubes. These properties are what finally define UCN.

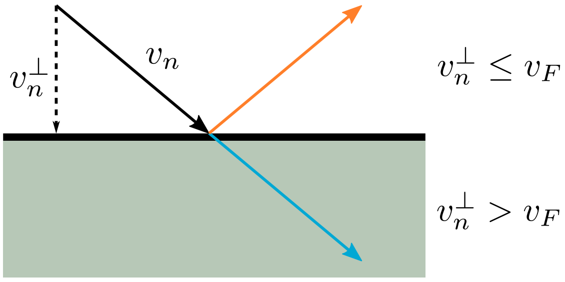

Figure 5 – Schematic representation of UCN reflection. Neutrons whose normal component of velocity (with respect to the material surface) is smaller than the Fermi velocity experience total reflection. In the other case they are transmitted through the material.

In practice, UCN sources always deal with either fission or nuclear reactions to meet the required high neutron densities. Even though the nature of neutron production through both mechanisms is quite different, the subsequent cooling down process is somewhat identical. Because the data collected for the present work was obtained from UCN generated at two different facilities, each employing one of the two discussed mechanisms, a brief description for both cases is presented.

1.3.1 UCN from spallation at PSI

Neutrons produced by this source come from the proton spallation of lead. PSI cyclotron accelerates protons at 590 MeV, with a beam current slightly higher than 2 mA. The beam operates in pulsed mode with kicks that last 8 s, every 300 s. Product of the proton-to-lead collisions, fast neutrons (~ 2 MeV) are generated at rates of about 10^{17} s^{-1} [11]. The first stage of neutron moderation is completed by 3.6 m^3 of heavy water surrounding the target at room temperature. At this point, neutrons reach thermal energies (~ 25 meV). Next, a solid deuterium crystal (sD$_2$) located in the middle of the heavy water tank with a temperature of about 6 K, continues the moderation process until leaving the neutrons with energies close to 10 meV. At this energy range, neutrons start interacting with the crystal as a whole rather than with the individual deuterium nuclei. They transfer their energy to the lattice via phonon excitation. After several scattering processes of this kind, neutrons emerge from the crystal with energies < 300 neV.

From this moment neutrons behave as UCN and hence are guided to a Diamond-Like Carbon coated vessel that stores them and leaves them ready to be "poured out" into experimental setups. The delivery of UCN is done using 8 m long guides that penetrate the biological shielding at two different areas. Figure 6 shows the spatial distribution of the main components described in the UCN source here.

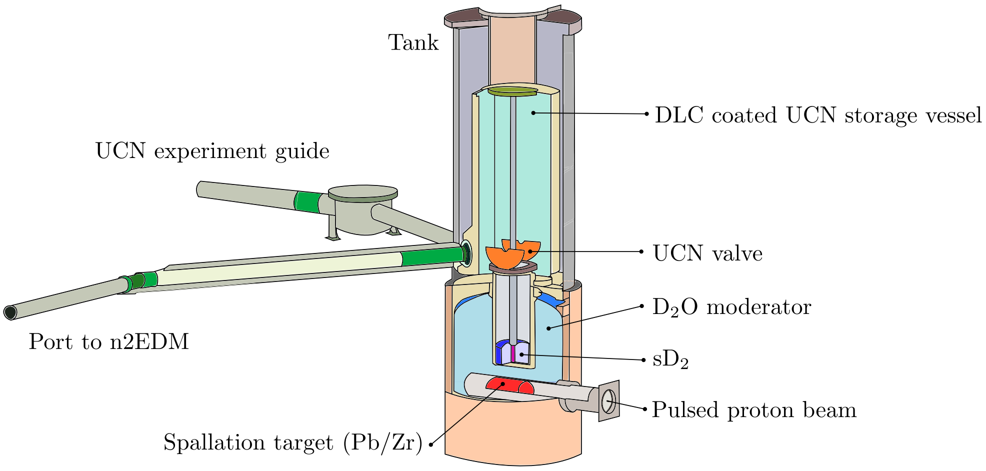

Figure 6 – UCN source at PSI in Villigen, Switzerland. The 7 m height tank houses the spallation Pb/Zr target, ~ 3.6 m^3 of heavy water (D_2O), ~ 30 dm^3 of sD_2 and the ~ 2 m^3 storage vessel (~ 2.5 m height). Figure adapted from [17].

1.3.2 UCN from fission at the Mainz TRIGA reactor

The second most common UCN source is nuclear reactors. Although any reactor can be used for such purpose, only the Triga Research Isotopes General Atomics (TRIGA[§]) Mark II reactor at the Institute für Kernchemie in Mainz will be explained.

[§] As a curiosity, this type of reactor was designed in such a way that accidents are almost impossible. Edward Teller, one of its inventors, said "could be given to a bunch of high school children to play with without any fear that they would get hurt" [18].

UCN are obtained from the TRIGA reactor (which is considered as a low-power reactor) in two different modes, one with constant neutron flux and the other in pulsed mode. While in the former, the reactor operates at a constant thermal power of 100 kW, in the latter, it reaches a peak power of 250 MW with a pulse width of 30 ms [19]. In either case, U-235 fission neutrons are firstly moderated by the heavy water in the reactor pool (see Figure 7). Out of the four beam tubes that penetrate the concrete shielding, two of them are reserved for the UCN production. This source also uses a sD_2 crystal to convert the thermal neutrons into UCN. A thermal bridge cools down the beam tube's front end, which walks the neutrons inside the crystal. The low temperature is maintained by means of a cryostat system based on liquid ^4He coolant. After finishing the cooling down process, UCN are transported through guides to the delivery area. Reported values show that rates in this facility go up to 240000 UCN per pulse, just outside the biological shield. UCN densities of about $\approx 10/\text{cm}^3$ are set aside in stainless-steel bottles [20].

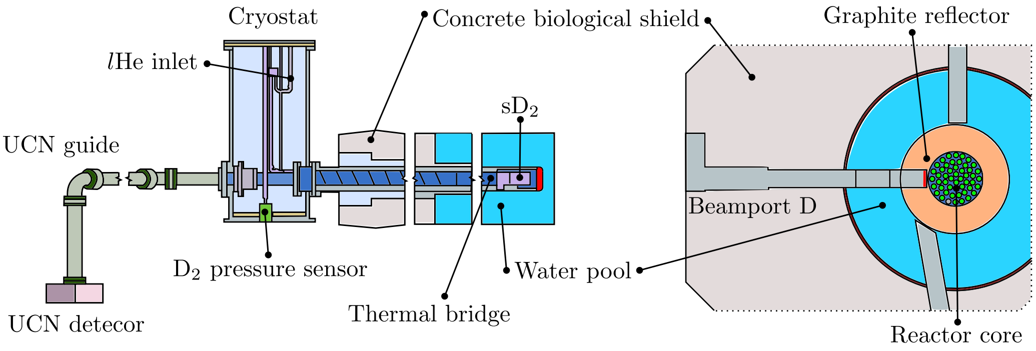

(side view) (top view)

Figure 7 – Top view of the TRIGA reactor beam tubes (right). UCN extraction is done across beamport D. The cryostat and sD_2 converter are shown from the side view (left). The distance between the reactor core and the exterior face of the concrete wall reaches 3 m for beamport D. Figure adapted from [20].

1.4 Detection of UCN

Since the discovery of the neutron in 1932 by Chadwick, detectors of these particles have been characterized by their indirect working principle. The zero net charge of neutrons excludes them from processes such as atomic excitation and ionization, that are the most exploited phenomena in particle detection. To circumvent this issue, the detection is achieved after a first conversion reaction. In general, it involves the neutron absorption followed by the emission of charged particles. These secondary particles travel while depositing their energies in a medium that produces a voltage signal, which in turn gives account of the neutron detection. Since the neutron energy is frequently much shorter than the reaction energy, information of the first is most of the time lost.

There are some features of UCN detectors that differentiate them from higher energy neutron detectors. Often, the sensitive volume size is smaller for the former since the absorption cross section becomes quite larger at such energies. Another difference is the existence of a critical velocity v_c for UCN [21]. This parameter is defined by the material composing the entrance window of the detector. In order to avoid UCN reflection, this first layer has to have a Fermi potential low enough so to allow the UCN transmission. Although several UCN detector types have been developed, it is crucial to compare their capabilities for nEDM experiments. There are three main requirements that should be fulfilled by the detectors to be regarded as suitable:

- The **UCN detection efficiency** plays an essential role in the future n2EDM experiment. As presented in equation 10, the uncertainty in the measurement of d_n is affected by the UCN counting (N_0) as

  $$\sigma_{d_n} \propto \frac{1}{\sqrt{N_0}} = \frac{1}{\sqrt{\varepsilon_{\text{det}} \cdot t_{\text{exp}} \cdot r_{\text{del}}}}, \tag{11}$$

  with ε_{det} the detector efficiency, t_{exp} the time duration of the experiment, and r_{del} the UCN delivering rate. This last quantity is entirely determined by the UCN source features, therefore if a certain σ_{d_n} is intended, the detection efficiency establishes how long the experiment should be. For instance, a 10% improvement in ε_{det} would represent an experiment 1/10 times shorter. In terms of money and human resources, this results crucial considering that from a 1-year run, one entire month could be saved[¶]. The ideal case is that in where all the UCNs crossing the detector entrance window undergo absorption. This is directly linked to the UCN *mean free path* (λ) and the detector's length (L), which allow to estimate the efficiency as [22]

  $$\varepsilon_{\text{det}}(E_{\text{ucn}}) = 1 - \exp\left[-L/\lambda(E_{\text{ucn}})\right], \tag{12}$$

[¶] That is the reason why a great effort is put in constructing a detector with an efficiency close to 100%.

in where E_{ucn} represents the UCN energy. Depending on the UCN absorption mechanism, the length L is chosen so to ensure $\varepsilon_{\mathrm{det}} \approx 100\%$. Not included in this expression but also affecting the efficiency are the losses due to UCN upscattering (example in Appendix A) and the presence of a dead layer after the UCN absorption region (the charged particles from the reaction never reach the ionizing volume).

- To benefit from the large UCN delivery fluxes, detectors should be able to process **high counting rates**. For instance, UCN rates can go up to $10^6 - 10^7$ c/s at the PSI facility [21]. Typically, this feature depends on the process through which the charged particles produce the voltage signals (ionization or scintillation).

- In order to diminish the background contribution, detectors should either have **low sensitivity to gamma-rays** or include a **effective events discrimination** (normally completed through spectroscopy or pulse shape analysis). It is the case that gamma background is predominant in solid detectors rather in gaseous ones.

In the following, a brief discussion of some UCN detectors tested and utilized in previous experiments.

1.4.1 ^{6}Li-doped glass scintillator

^{6}Li glass scintillator, known in the literature as GSx, contains Ce_2O_3, SiO_2, MgO, Al_2O_3 and Li_2O oxides. It takes advantage of the ^{6}Li isotopes to capture neutrons ($\sigma_a = 344667$ bar[‖]) via the reaction

$$\mathrm{n} + {}^6\mathrm{Li} \rightarrow {}^3\mathrm{H}\ (2.74\ \mathrm{MeV}) + {}^4\mathrm{He}\ (2.05\ \mathrm{MeV}). \tag{13}$$

The emitted products, whose energies amount to 4.79 MeV[**], trigger the scintillating process after ionizing the Ce atoms (Ce^{3+}). Recalling that nEDM experiments demand a high UCN counting rate, this detector is a good choice given the fast decay time 60-75 ns of the light-emitting states [23]. The scintillated light is characterized with a maximum wavelength at 395 nm for all the GSx types [24].

[‖] Value scaled from thermal energies with the $1/v$ law: $\sigma_{\mathrm{UCN}} = \sigma_{\mathrm{th}} \times v_{\mathrm{th}}/v_{\mathrm{UCN}}$.

[**] This available energy benefits the discrimination of neutrons against the background, mainly composed of gamma-radiation.

The particularity of this detector is found in its double-layer configuration, specially designed for UCN detection in the first phase of the nEDM project. As shown in Figure 8, the glass front face is ^{6}Li-depleted (GS3 or GS30) while the remaining portion is ^{6}Li-doped (GS10 or GS20). Such partitioning reduces the probability of escape events that give place to partial energy deposition counts ($E_{\text{det}} < 4.79$ MeV). Since the first layer is almost transparent to UCN, neutron capture is more likely in the second one. Therefore, tritium and helium energy deposition tracks start rather at the inner glass region. One drawback of this detector is its sensitivity to gamma background. Compared with gaseous detectors, the cross section for gamma-ray interaction is larger for crystal materials.

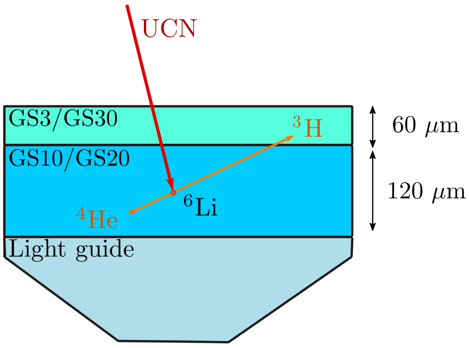

Figure 8 – Graphical representation of UCN interaction in the ^{6}Li-doped glass scintillator. The first ^{6}Li-depleted layer (GS3 or GS30), transparent to UCN, avoids the escape of the reaction products. Following, a ^{6}Li-doped layer (GS10 or GS20), in charge of the UCN absorption. The scintillated photons are collected at the end of the light guide (bottom part).

1.4.2 Cascade detector

This kind of detector is based on the ^{10}B neutron capture. The large UCN absorption cross section of boron ($\sigma_a = 1.4 \times 10^6$ barn) is used to stop neutrons in a 100 μm thick layer via the reactions

$$\mathrm{n} + {}^{10}\mathrm{B} \rightarrow {}^{11}\mathrm{B} \rightarrow {}^{7}\mathrm{Li}^{*} + {}^{4}\mathrm{He}\ (\sim 94\%), \tag{14}$$

$$\mathrm{n} + {}^{10}\mathrm{B} \rightarrow {}^{11}\mathrm{B} \rightarrow {}^{7}\mathrm{Li} + {}^{4}\mathrm{He}\ (\sim 6\%). \tag{15}$$

The ^{7}Li and ^{4}He are emitted with kinetic energies near 1.47 MeV and 0.84 MeV, respectively, that subsequently are deposited in an argon-CO$_2$ gas mixture through ionization processes. The reaction product's tracks, whose lengths are in the order of a few mm at atmospheric pressure [25], give place to a cascade effect when the primary electrons are drifted towards the wholes in a gas electron multiplier (GEM) foil[††]. In here, the number of electrons is amplified by means of a potential difference supplied at both sides of the foil. The electron cloud coming from the wholes is detected with a readout 2D structure, composed of 256 pixels in a total area of 200 mm^2. Figure 9 sketches the main elements in the detection chain. Because the UCN conversion and the ionization occur in different regions, this detector is characterized with a dead layer. Around 10-15% of the reaction products are totally absorbed within the finite thickness boron layer and lost from the counting electronics. A second drawback of this detector is its lack to perform discrimination through spectroscopy or pulse shape analysis.

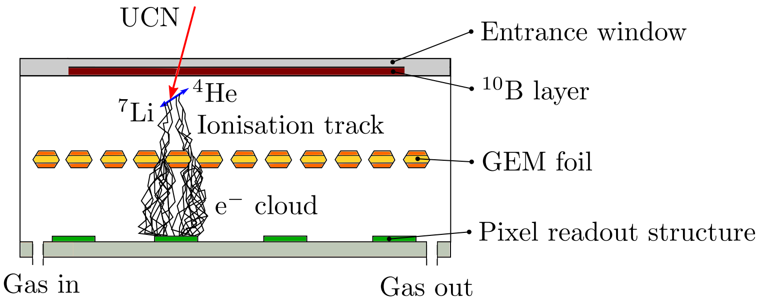

Figure 9 – Basic representation of the working principle in a cascade detector. The number of primary electrons is increased after passing through the GEM foil. The Ar-CO−2 gas mixture circulates in continuous mode to minimize aging effects.

1.4.3 ^{3}He gaseous detector (Strelkov)

^{3}He based detectors have been widely used in neutron experiments [26, 27, 28]. In the energy range of UCN, the ^{3}He absorption cross section is even larger than that of ^{10}B ($\sigma_{\mathrm{ab},^{10}\mathrm{B}} \approx 0.8\sigma_{\mathrm{ab},^{3}\mathrm{He}}$). However, since ^{3}He is used in a gaseous state, the detector's sensitive volume is larger than of the cascade detector.

The detection mechanism follows the reaction

$$\mathrm{n} + {}^3\mathrm{He} \rightarrow {}^1\mathrm{H} + {}^3\mathrm{H} + 764\ \mathrm{keV}, \tag{16}$$

in where the released energy is distributed as 573 keV for the proton (^{1}H) and 191 keV for the tritium (^{3}H). A second gas, that has been fed into the

---

[††] Normally, a GEM is a 50 μm tick kapton foil, copper clad on each side.

same gas chamber as the ^{3}He, works as a stopper of the reaction products. The energy deposition occurs through ionization of the stopper, which release electrons that are collected by a high-voltage wire electrode, located at the bottom of the chamber (see Figure 10). In the literature, detectors that operate according to this mechanism are known as Strelkov detectors.

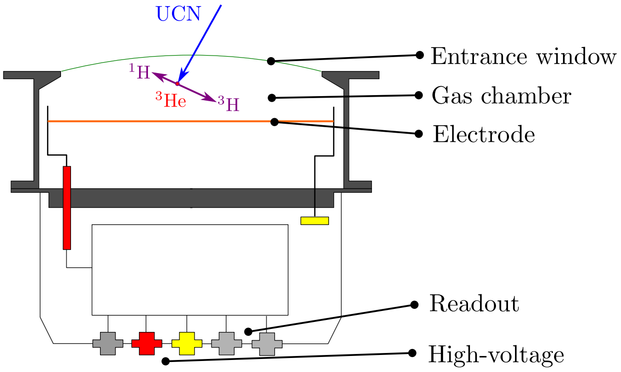

Figure 10 – Diagram of a Strelkov ^{3}He detector. Figure adapted from [21].

In principle, Strelkov detectors can be operated with any ionizable gas mixture that has a stopping power strong enough. Among the already implemented alternatives, there are Ar-CO_2, Ar-CH_4 and CF_4, all showing different performances depending on the gas pressure. Independently of the choice, the duration of the pulse signals is determined by the charge collection process, which results in the order of a couple μs. This last feature represents one of the main limitations of the detector when high counting rates are aimed [21].

2 GADGET: A novel UCN gaseous detector

Just as the Strelkov detector described in section 1.4.3, the GADGET prototype, firstly reported in this work, uses the ^{3}He gas as a neutron absorber. The main difference relies on the conversion method. Whereas detection in the Strelkov model is achieved by the collection of electrons released from the ionization, the GADGET type collects the photons emitted from the same process. In other words, the novel model is the scintillating version of the Strelkov detector. Although gases such as Ar, Xe, Kr, N_2, CH_4 and CO_2 are used as scintillators in proportional counters of charged particles [29], GADGET is operated with CF_4 gas only. The justification for such selection will be later addressed. For the moment, let us present a detailed explanation of the detector in question.

2.1 Working principle and technical details

The UCN detection in GADGET is described by a chain of processes that starts with the neutron absorption and finishes with light collection. There are two intermediate entities between the first and last steps: ^{3}He and CF_4 gases. UCN are absorbed by ^{3}He nuclei through exothermic reactions that produce two new particles, namely, proton and tritium, plus 764 keV* (see equation 16). The second step consists in the energy deposition of the reaction products in the CF_4 gas; CF_4 molecules are either ionized or excited. Then, light is emitted from electron recombination and de-excitation of the CF_4^* states, whose lifetimes are close to 6 ns [30].

The ^{3}He and CF_4 gases are stored in a cylindrical stainless-steel chamber with a volume of $\pi \times 7.4^2 \times 8.9$ cm^3 (see Figure 11). An entrance window dedicated to the UCN access is located in the upper wall. It holds a 30 μm foil made of $Al_{97}Mg_3$ alloy, whose circular shape matches the standard UCN guide dimensions (further details on the foil and entrance window are found in section 2.4).

Following the ionization/excitation processes, the emitted photons travel inside the chamber until finding one of the three light output windows (targeting the PM tubes) or the stainless-steel chamber walls. In the latter case, photons can be either absorbed or reflected towards an output window or

---

*This value represents the mass difference between products and reactants. UCN kinetic energy is neglected ($E_{\text{ucn}} \sim 300$ neV $\ll Q$).

another wall. To enhance the light reflection, the inner faces of the chamber have been polished. When photons reach one of the output windows, they find a circular quartz layer with 6 mm thickness, conveniently transparent to the wavelengths emitted from CF_4 (see next section). On the other side of each quartz layer, PM tubes are mechanically coupled with the help of silicone optical grease (BC-630) that improves the light transmission.

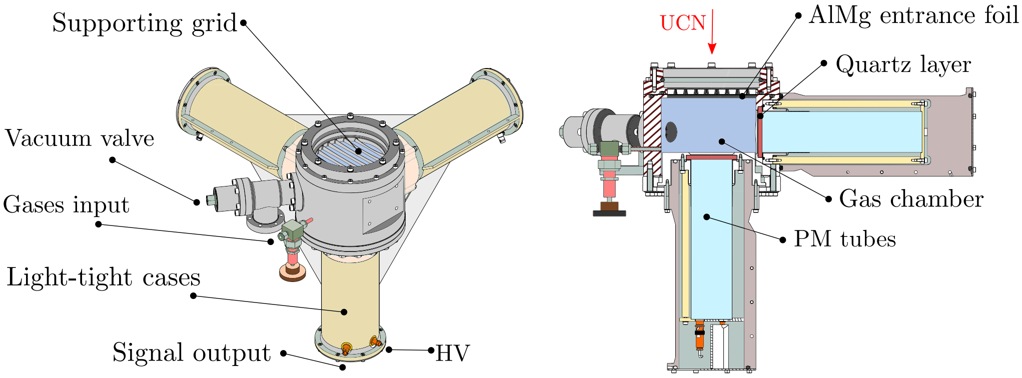

Figure 11 – Scale drawing of the GADGET prototype indicating its mains components. The left side shows a 3D-view of the already mounted detector. On the right, a sectional view allows seeing inside the cases and chamber. The red arrow indicates the direction of UCN entering the chamber. Technical drawing from [31].

2.2 Light emission/collection

Among scintillating gases, CF_4 is chosen in virtue of its high photon yield, transparency to its emitted light, non-flammability, accessible and price. Previous studies have proved that CF_4 photon yield spectrum, resulting from α irradiation, depends on the gas pressure (P_{CF_4}) [32, 33]. As shown in Figure 12, the emitted photon wavelengths range from 200 to 800 nm, with peaks at $230, 300$ and 630 nm. The total yield, integrated in the whole range at 1 bar, results in ~ 2683 ph/MeV. With this value, and assuming that the light emission from α irradiation is equivalent to that induced from proton and tritium ionization, the total photon yield per UCN absorbed can be estimated as

$$\frac{\text{total ph. yield}}{\text{UCN}} = \frac{\text{ph. yield}}{\text{MeV}}(K_{^1\text{H}} + K_{^3\text{H}}) \approx 2683\frac{\text{ph}}{\text{MeV}}(0.573 + 0.191)\ \text{MeV} \tag{17}$$

$$= 2050\ \text{ph}. \tag{18}$$

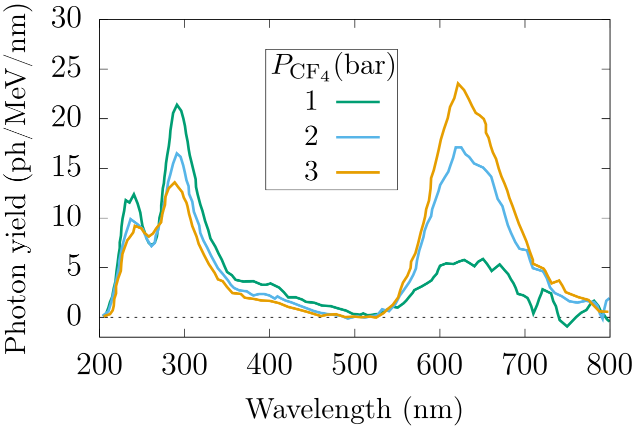

Figure 12 – CF_4 photon yield from α irradiation. Short wavelengths (200-300 nm) light emission decreases at high gas pressures. The opposite behavior is seen at large wavelengths (550-700 nm). Data points taken from [33].

Several details need to be considered when setting the CF_4 pressure in the GADGET detection chamber. A first estimate of the required CF_4 pressure is calculated from the reaction products slowing-down process. The goal is to determine what pressure would ensure a complete halt of the reaction products. To this end, the SRIM software [34] is used to calculate the range of proton and tritium inside a CF_4 gaseous medium, with energies specified by the UCN+^{3}He reaction. In Figure 13, the output of this simulation at different CF_4 pressures is presented for the two particles. The first conclusion is that, even at pressures as low as 200 mbar, both reaction products are stopped given that their creation (UCN absorption point) takes place at least 2.3 cm apart from the chamber walls.

This being said, no matter what CF_4 pressure is used, there will always be a probability different from zero that one of the reaction products reaches the detector walls. This due to the fact that UCN absorption is a probabilistic phenomenon that can occur in the vicinity of the walls (especially the detector's entrance window). The reaction product deposits part of its energy in the gas and the rest in the wall. Since only the former involves the emission of scintillating light, the mean photon yield in the chamber is reduced, and the event appears as coming from a less exothermic UCN reaction. Consequently, in an energy spectrum, such events (frequently referred to as escape or edge events) are stacked on a continuous region with energies $E < 0.764$ MeV.

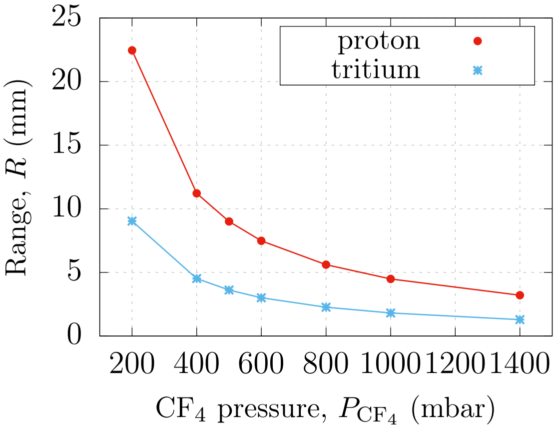

Figure 13 – Proton and tritium ranges in CF$_4$. Data points calculated with SRIM software at different gas pressures.

Figure 14 shows a Geant4-simulated energy spectrum of a detector with perfect resolution. The sensitive volume consist of a cylinder with the dimensions of GADGET's gas chamber. It is filled with CF$_4$ at 200 mbar and ^{3}He at 15 mbar, and surrounded with an aluminum layer. The histograms are constructed with the total energy deposited by the reaction products in the gas mixture. This figure shows the contribution of each edge-events type to the total distribution. The "stairs" shape is product of the ^{1}H and ^{3}H complete escape events, they reduce the deposited energy by 573 keV and 191 keV, respectively. It can also occur that both particles reach the walls ("double escape"); however, this is a less likely process since the UCN absorption has to occur near the chamber corners. Another point to mention is the evidence of a second type of escape included in the "no escape" spectrum. Although the reaction products are totally stopped, some of the ionized electrons are not (electron escape). They correspond to the yellow counts with $E \simeq Q$.

Regarding the last step in the detection chain, that is the photon collection, GADGET gas chamber counts with three ⌀6.2 cm cavities at the end of the light output windows. They were especially designed to house the 2-inches bialkali photocathode R1828-01 Hamamatsu model [35]. Its sensitivity to wavelengths ranging from 290 nm to 700 nm, with a maximum quantum efficiency of $\sim 30\%$ at 380 nm, converts it in a right choice recalling that the CF$_4$ emission lays in the same wavelength range (see Figure 12).

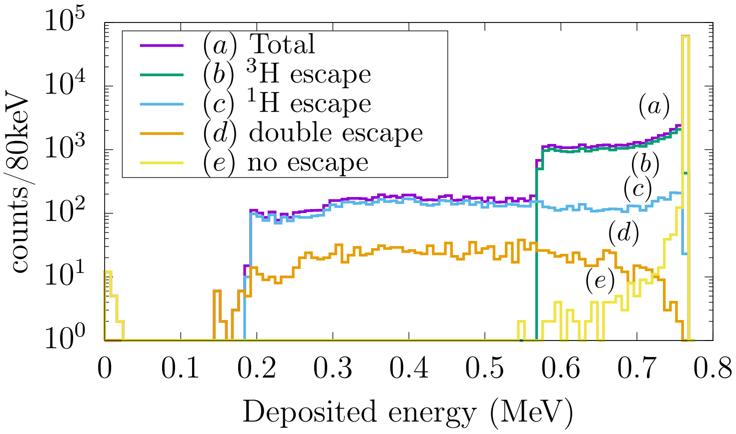

Figure 14 – Geant4 simulated energy spectrum. The histogram is constructed with the energy deposited by the reaction products in the gas (perfect resolution is assumed). Simulation of 10^5 UCN impinging normally through the entrance window into the chamber, filled up with CF_4 at 200 mbar and ^{3}He at 15 mbar. With colors the different contributions to the total detection.

2.3 Data acquisition with FASTER system

The voltage signals generated by the PMs are processed with the Fast Acquisition SysTem for nucleEar Research (FASTER) developed at *Laboratoire de Physique Corpusculaire* (LPC) in Caen [36]. This digital data acquisition system is based on Field Programmable Gate Arrays (FPGA) whose hardware components are designed in a modular fashion. The FASTER unit module consists of a motherboard hosting two daughter boards each equipped with two analog-to-digital converters, both characterized with a sampling capacity of up to 500 MHz with 12-bits.

The signal treatment, carried out in the FPGA, includes baseline restoration (BLR), low and high pass filters, 2-dimensional threshold triggering, charge integration, among others. The parameters defining these tools are easily manipulated from the visual interface offered by the software *faster_gui*, also developed by the FASTER LPC team. Essential for the GADGET detector is the single clock system, which is synchronized for all the channels (all the PMs). It allows storing the absolute time of each event with a 2 ns resolution.

2.3.1 Two-dimensional trigger

The definition of what a "pulse" is comes from the trigger settings. Among the possible options in FASTER modules, the two-dimensional trigger is chosen. It is activated when a signal crosses a threshold level V_{th} and maintain above it for a period longer than t_{th}. Figure 15 shows an example of a pulse fulfilling such conditions. Apart from noise suppression, trigger settings are commonly used as a first background filter. When the desired events are well defined, meaning known amplitude and time duration, the two-dimensional trigger results in an efficient tool for rejecting events with little charge deposition or fast decay time (as for instance the Cherenkov detection pulses).

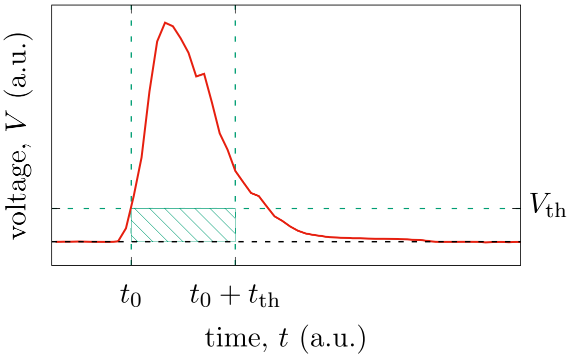

Figure 15 – Two-dimensional trigger visualization. Pulses are processed if the signal overcomes V_{th} during a time longer than t_{th}.

2.3.2 Triple coincidence

The coincidence technique has a dual-purpose in the GADGET detector, these are the recording of complementary light signals and the differentiation of non-UCN events. The assumption is that UCN absorption should produce enough scintillating light so that the three PMs are triggered almost simultaneously (within a short time window). Those events are labeled with a 'group' indicator and are said to be *in coincidence*. On the contrary, events detected alone, by one PM only, are attributed to phenomena originated outside the gas chamber (single background events) and do not receive any particular label.

Data grouping with FASTER software is executed either in real-time (during the data recording) or after the experiment. In both cases, it results convenient to examine a reasonable time length τ_{group} for the window that defines the coincidences (group events). For this purpose, three main processes need to be looked at: the time required to stop the reaction products and ionized electrons, the lifetime of the CF_4 excited states, and the time for the light to travel inside the gas chamber. In the first case, a rough approximation can be obtained from the ranges and energies of the particles

$$t_{\text{stop}} \approx \frac{R}{v} = \frac{R}{\sqrt{2K/m}}, \tag{19}$$

that results in ~ 2 ns for proton and tritium. A bit longer is the CF_4^* lifetime, $\tau_{\text{CF}_4} \approx 6$ ns (see section 2.1), but the fastest happens to be the travel time of light, calculated from the chamber diameter as

$$t_{\text{travel}} \approx \frac{D}{c} \approx \frac{0.148 \text{ m}}{c} = 0.5 \text{ ns}. \tag{20}$$

Thus, a time window with $\tau_{\text{group}} \gtrsim 10$ ns should be enough to give the three PMs the opportunity to be triggered. In section 3.2.2, the time distribution of events inside coincidence groups, obtained from UCN detection, will be used to validate this statement.

So far, the discussion has been restricted to the event's time distribution; however, information from the voltage pulses is what allows one to complete the counting and discrimination of UCN events. In particular, from gamma events that may occur in the gas chamber and induce a undesired coincidence event. From the FASTER system, two acquisition modules are convenient for this purpose, namely the QDC and SAMPLER modules.

2.3.3 QDC module

PMs produce voltage pulses whose shape and duration depend on the type of process generating them. One way to study these quantities is through the area of the waveform. The QDC module computes the pulse integration into up to four different time windows, known as gates (see Figure 16). If the time-sampled voltage signal is denoted as $V(t)$, the QDC calculation performed in the digital module is expressed as

$$\text{QDC} = \sum_{t=\text{gate start}}^{t=\text{gate end}} V(t). \tag{21}$$

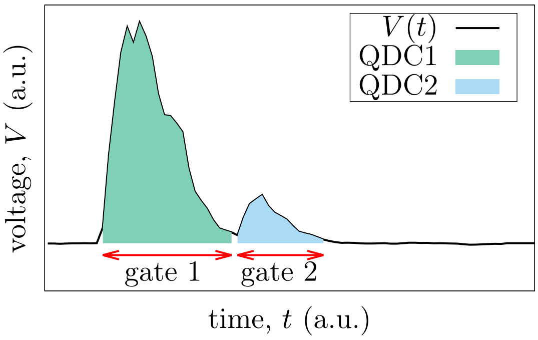

Figure 16 – Representation of the QDC module working principle. In this pulse sample, two gates are used to calculate the charge (QDC1 and QDC2) at different time ranges.

Adjustment of the *start* and *end* times for all gates is possible through the visual interface. If no previous information of the pulse shape is available, it is recommended to define the gates just before the experiment using the oscilloscope provided within FASTER modules. Since the waveforms generated by the PMs in GADGET follow an erratic behavior[†], the QDC range should be made long enough so to cover the whole pulses without cutting their tails.

2.3.4 SAMPLER module

Given that the QDC module is able to store the integrated charge but not the entire pulse, part of its information is missed. This issue does not represent a problem for experiments in where the amplitude or width of the pulses are irrelevant. However, it is the case that Pulse Shape Discrimination (PSD) based on those parameters is useful to differentiate UCN detection from other in-chamber generated events. Thus, in order to explore the differences between pulses, the SAMPLER module is used to record the whole waveforms for all coincidence events.

Depending on the gate width, which can be fixed by the user or automatically defined by the pulse duration, the number of points per waveform can be as large as 714 (1428 ns). It is evident that with this data structure, any pulse shape analysis can be done in a post-experiment stage. However, when the events rate is too high, the amount of data to be transmitted becomes

---

[†] The number of photons generating the signals is not large enough to produce pulses with well-decaying shapes.

massive and cannot be handled by the acquisition system, resulting in data losses. Therefore, for the present work, the SAMPLER module was only used to perform a study of the pulse shapes (the detector efficiency measurements were performed with the QDC module).

2.4 Entrance window

One of the most decisive factors in the UCN counting efficiency, for all types of detectors, is the entrance window. Just as the reflection experienced by UCN at the inner sides of the transporting guides, the first layer of every detector can behave as a mirror if its Fermi potential is too large. Due to this issue, different alloys and thicknesses have been tested so to establish what entrance foil enhances UCN transmission the most (see Table 2). It is observed that, in general, the thinner the foil, the higher the transmission. As for the material, the aluminum-magnesium alloy exhibits the highest transmission at the different thicknesses.

Table 2 – UCN transmission through thin foils used at the entrance window of gaseous detectors. Values reported by [37].

Material	Thickness (μm)	Transmission (%)
Al	100	77.40
	50	88.46
	25	91.64
$Al_{97}Mg_3$	100	81.68
	60	87.08
	30	92.94
Al_6O_6	100	78.49
Ti	50	45.03
	25	65.29
$Ti_{90}Al_6V_4$	50	49.20

As a technicality, the entrance foil can not be made excessively thin without considering the pressure difference that it experiences. On one side, UCN guides are vacuumed at pressures below 10^{-6} bar, while on the other CF_4 is fed into the chamber with pressures of about 1 bar. To circumvent this issue, GADGET was designed in such a way that a metallic grid can be placed on top of the foil to provide mechanical support. Currently, this grid makes possible the use of aluminum layers as thin as ~ 15 μm.

3 Performance at the PSI UCN source

The first test of the GADGET prototype with UCN took place at PSI in December 2018. The main task of this experience was to evaluate the operating of the entire apparatus, from gas feeding to data storage. Secondly, in order to explore the optimal working conditions, UCN detection and background influence were tested at different gas pressures. Also, at the acquisition level, triggering and grouping parameters were shifted to appreciate their effects on the detection efficiency.

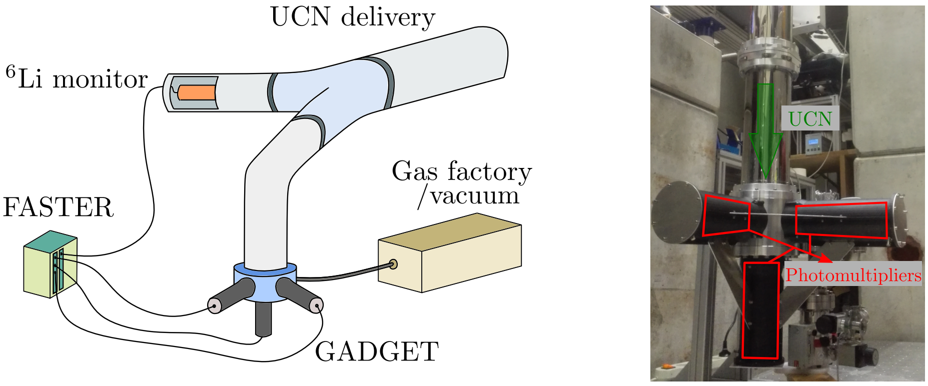

Figure 17 – Schemme of the experimental setup at PSI. GADGET and a ^{6}Li-based (monitor) detectors are place in the ends of a forked UCN guide. UCN reach the gas chamber after a fall of about 1 m.

As mentioned in section 1.3.1, PSI UCN source operates in pulsed mode. Moreover, because the peak has shown a maximum that changes from pulse to pulse, the UCN flux needs to be monitored if one wants to compare the GADGET performance at different conditions. The monitoring is completed by a ^{6}Li-based detector, placed in one of the two ends of the UCN delivery guide (see Figure 17). Due to the geometrical limitations of the arrangement, the altitudes of both detectors are not identical. While the monitor was at the level of the entrance guide, GADGET was positioned $\sim$ 1 m below them. In the last case, UCN are conducted through an elbow joint to a vertical guide, in where they experience a 1 m free fall* before entering the gas chamber.

---

*Due to the gravitational field ($V_g = m_n g h$), UCN gain about 102 neV/m.

3.1 UCN monitor counts

Monitoring counts are managed by a ^{6}Li-dopped GS3/GS20 detector; as the one introduced in section 1.4.1. In practice, it records up to 7×10^{3} counts per second at the pulse maximum, which occurs a couple of seconds after the proton beam shut down (see Figure 18). After the peak, the counting rate decreases exponentially until the next beam pulse starts the cycle again. The small peak observed before the beam pulse is produced by a quick testing proton beam used to align the beam direction on the lead target.

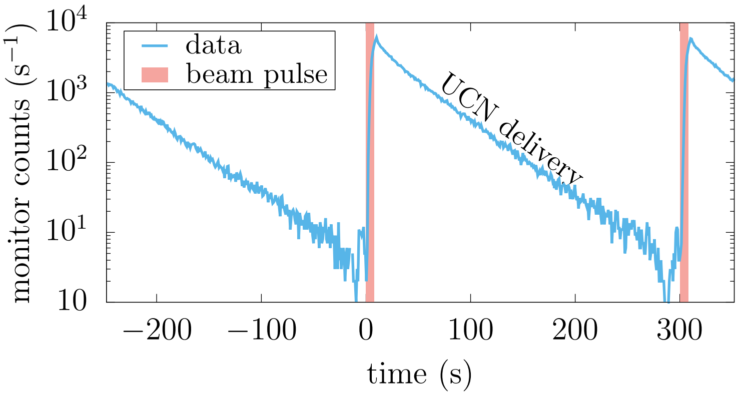

Figure 18 – Raw counting rate for monitor detector at PSI. The proton beam is activated for 8 s every 300 s. UCN delivery to experiments is possible during all the pulse. Data shown represents the overall counting.

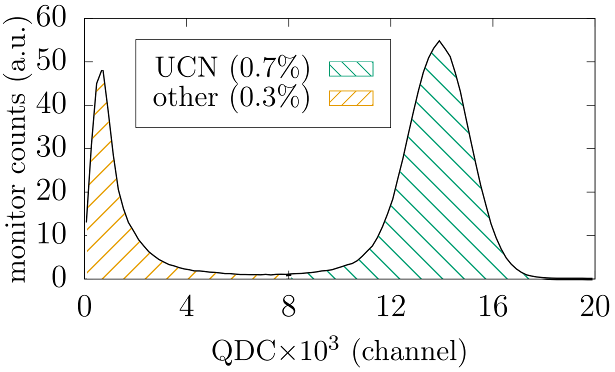

Figure 19 – Integrated charge spectrum for monitor detector at PSI. Events recorded during one pulse cycle. UCN are distributed in the right green region. Other events, as gamma background, Cherenkov and electric noise, located on the left region [23].

Part of the monitor counts, measured along the entire cycle, comes from non-UCN events. Most of them are easily distinguished in QDC spectra (see Figure 19). While full-energy UCN capture generates a well-defined peak at large charges, other events accumulate in the low charge region. In this way, setting a QDC limit condition ($\text{QDC} > 8 \times 10^3$) is enough to filter out gamma interaction, Cherenkov events, and electric noise [23]. Taking into account that these background events represent about 30% of the total spectrum, the actual UCN counting rate at the maximum of the pulse is estimated at 4.9 $\times 10^3$ s^{-1}. It will be seen in the next sections that the integral of this counting rate is used to normalize the counts of the GADGET detector.

3.2 QDC and time spectra with GADGET

With GADGET each PM records a QDC value every time a voltage pulse fulfills the threshold conditions. The magnitude of this charge is related to the size of the gate. A tiny gate would miss part of the pulse, while a huge one would include noise and increase the dead time. Therefore, sample pulses created by UCN events need to be revised to define accurately the time integration range.

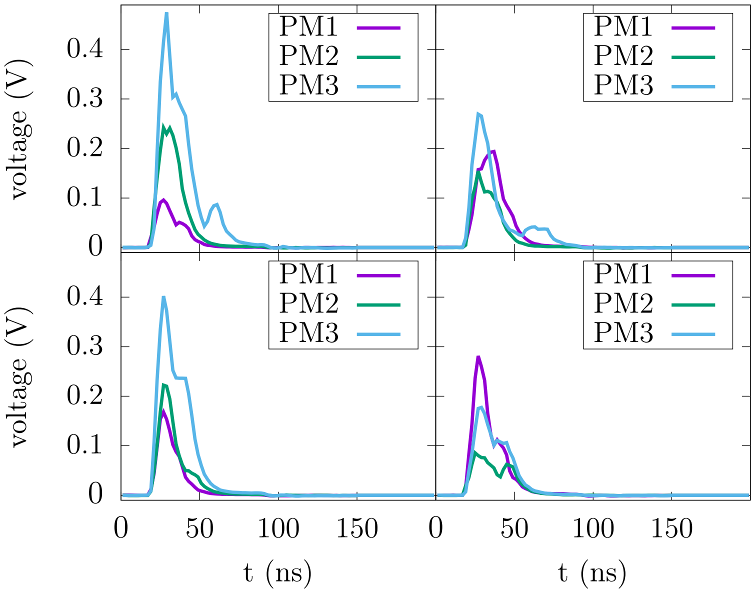

Figure 20 – Four coincidence events sampled some seconds after the proton beam kick (UCN events) with the GADGET detector.

Figure 20 shows four typical coincidence events recorded with GADGET.

Several observations can be made out of them. First, pulse shapes do not follow a definite pattern, one pulse can have multiple maxima and minima. This is explained after the low number of photons produced per UCN detected. Also, the relative amplitudes change from event to event; the largest pulse is not always measured by the same PM (the amount of light seen by each PM depends strongly on the UCN absorption position). Last and most important, a QDC gate of 100 ns, counted from the pulse starting point, covers the entire signal independently of the shape and the PM producing it.

3.2.1 Individual counts

Depending on the gas pressures and other operating conditions, the overall counting rates registered by the PMs can reach several tens of thousands per second ($\sim 8 \times 10^4$ s^{-1} near the beam pulse peak). Indeed, a fraction of them corresponds to events produced within the PMs (gammas and electric noise), while the rest to events come from the gas chamber (gamma, UCN or any ionizing particle). Since only for the first case, the event is seen by a single PM, the corresponding entry in the storage file will not be correlated in time with any other signal. Therefore, events that originated inside the PMs and the gas chamber are easily resolved with the coincidence technique.

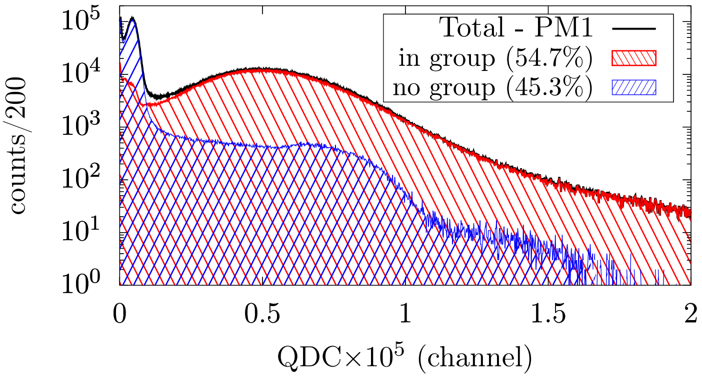

Figure 21 – QDC spectrum constructed with PM1 counts. Inside group (coincidence) and individual events are differentiated with the red and blue histograms, respectively. CF_4 pressure set at 1000 bar and ^{3}He at 15 mbar.

Figure 21 shows a first QDC spectrum obtained with PM1. The total distribution is composed of coincidence (in group) and single events (no group) with almost the same occurrence. However, it is observed that the single ones accumulate at low charges, just as expected from gamma-rays and electric noise. On the other hand, grouped events extend over the whole QDC range, exhibiting a broad peak centered around channel 0.5×10^5. This classification also suggests that near 45.3% of the total counts correspond to single events. Although this percentage represents a significant fraction of the data, it should be said that it is due to the threshold parameters which have been chosen in order to record all events.

The triple coincidence technique determines indeed a very stringent filter for single events. Evidence of this is the accidental counting rate (ACR). It estimates the rate of coincidence events originated from uncorrelated processes. One example would be the detection of electric noise in PM1 with detection of CF_4 scintillating light in PM2 and PM3. In such cases the ACR is calculated as [38]

$$\mathrm{ACR} = 3 C_{\mathrm{PM1}} C_{\mathrm{PM2}} C_{\mathrm{PM3}} \tau_{\mathrm{group}}^2, \tag{22}$$

in where C_i corresponds to the rate of uncorrelated events seen by i, and τ_{group} is the grouping time window introduced in section 2.3.2. Now, in the most conservative scenario, assuming that all events detected near the beam pulse peak come from uncorrelated processes:

$$C_i = 8 \times 10^4 \ \mathrm{s}^{-1} \tag{23}$$

for $i =$ PM1, PM2 and PM3, then, for a coincidence window of 200 ns

$$\mathrm{ACR} = 3(8 \times 10^4 \ \mathrm{s}^{-1})^3 (2 \times 10^{-7} \ \mathrm{s})^2 \approx 80 \ \mathrm{s}^{-1}. \tag{24}$$

It comes to the view that even at the beam pulse maximum, the accidentals are less than 0.1% of the total counts. On top of that, once the PSD is included, these events are easily rejected (see discussion about the 'noise' region in section 3.4).

3.2.2 In-coincidence counts

FASTER provides a complete description of group events, enabling one to manipulate parameters such as relative time, absolute time, QDC, size of the group, among others. For the sake of good order, let us start with the time distribution of events inside the groups. This first study has the purpose of determining how delayed the second and third events are with respect to the first one. Figure 22 shows the time distribution of coincidence events. The groups are constructed from data collected during 25 s after the proton beam kick. For that particular run, the gas pressure in the chamber was set in 1000 mbar and 15 mbar for CF_4 and ^{3}He, respectively. Although the coincidence time window was adjusted to 200 ns, it can be seen that $\tau_{\text{group}} = 60$ ns is enough to include most ($\sim 99\%$) of the 2nd and 3rd events. The remaining counts in the flat tails ($\sim 1\%$) are attributed to uncorrelated events.

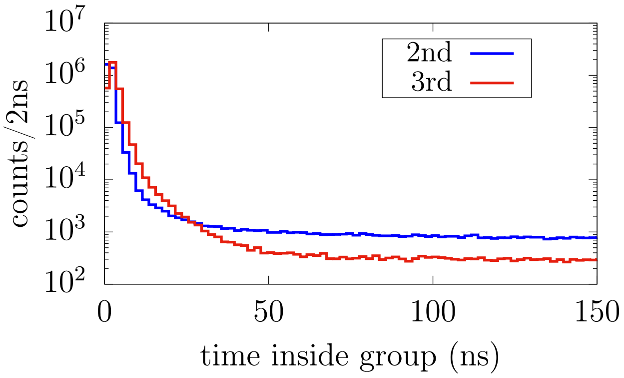

Figure 22 – Time distribution of second and third events inside coincidence groups. The time is measured with respect to the absolute time of the first event. The fast decrease of counts at large times suggests a coincidence window with $\tau_{\text{group}} = 60$ ns.

The following discussion concerns the QDC distribution inside the coincidence groups. As previously stated, the integrated charge of a pulse with origin in the gas chamber is not identical for all PMs. The UCN absorption position determines three effective solid angles covered by the gas output windows (PMs input windows). The larger the solid angle, the higher the voltage pulse and consequently, the larger the QDC.

Despite the differences induced by this geometric effect, once the three PMs are triggered in coincidence, the calculated QDCs still represent a fraction of the total light emission, i.e., they are complementary to each other. For this reason, it comes naturally to define the grouped QDC

$$\mathrm{QDC}_{\text{group}} = \sum_i \mathrm{QDC}_{\mathrm{PM}i}, \tag{25}$$

in where the sum runs over the three PMs. Given that more photons participate in the overall calculation, there is a significant gain in the energy resolution.

In order to appreciate the advantages of using $\mathrm{QDC}_{\mathrm{group}}$ rather than the individual contributions, both kinds of spectra are plotted and compared in Figure 23. As a direct consequence of summing the individual charges, the $\mathrm{QDC}_{\mathrm{group}}$ spectrum is spread in a range three times larger than the one for $\mathrm{QDC}_{\mathrm{PM}i}$. This amplification in turn allows a better identification of the different regions characterizing the spectrum. In particular, it is of great interest the $\mathrm{QDC}_{\mathrm{group}}$ region between channels 0.2×10^5 and 10^5, raised by edge events and gamma interaction, and between channels 10^5 and 3×10^5, associated to full-energy UCN.

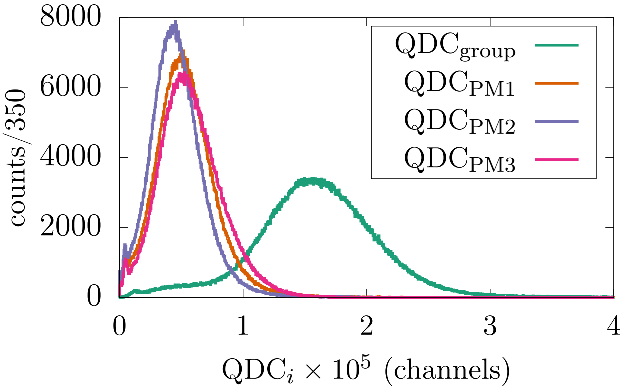

Figure 23 – In-coincidence charge spectra. $\mathrm{QDC}_{\mathrm{group}}$ is obtained as the sum, group by group, of the individual PMs contributions (equation 25). Since events come from the same coincidence groups, all the histograms have identical areas.

3.2.3 Double and triple coincidences

During the grouping process there might appear two cases that have not yet been considered, they are groups with two or more than three events. While the latter is discarded with the proper acquisition system settings (once a group has three events, it is closed and a new one is started), the former has a probability different from zero to occur. Figure 24 shows the charge spectra of groups raised by two and three coinciding events. It is evident that double groups, regardless of what pair of PMs record the signals, account majorly for low charge events. Indeed, since their distributions (b, c and d) do not show a UCN-kind peak, they are attributed to accidentals of single events from noise. In addition, the total number of counts reported in Figure 24 reveal that double groups represent less than 1.5% the number of triple events. For such reason, it is concluded that no UCN information is lost if the analysis is focused on the PM1-PM2-PM3 coincidence groups.

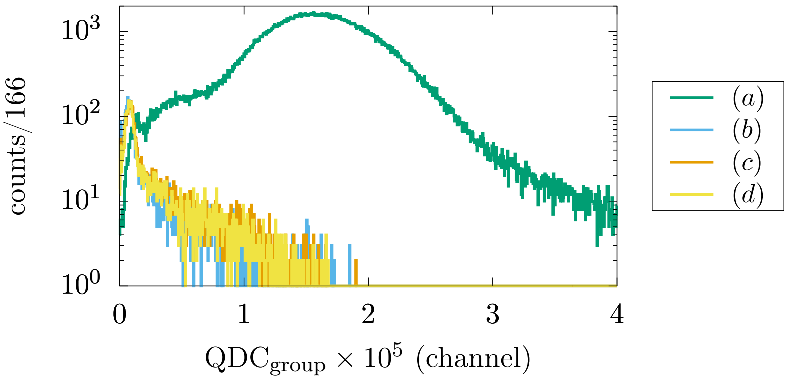

label	group	total counts
(a)	PM1-PM2-PM3	1055720(1027)
(b)	PM1-PM2	11952(109)
(c)	PM1-PM3	13200(115)
(d)	PM2-PM3	12219(110)

Figure 24 – Triple (a) and double $(b, c$ and $d)$ coincidence charge spectra. The total number of counts and the shape distribution reveal that double event groups, independently of what PMs are triggered, represent less than 1.5% of the triple event groups.

3.3 Background at PSI

As in any measurement, background contribution to events counting has to be estimated so to validate the final assertions. It has been already shown that the triple coincidence technique reduces accidental counts of single events to less than 1% of the total counting rate. Therefore, it only remains the evaluation of background events produced from within the gas chamber. The identification of other processes different from UCN absorption is conveniently accomplished either by removing the ^{3}He gas from the chamber or by closing the valve that lets the UCN flow into the delivery guide. This valve is located between the storage vessel and the UCN experiment guide (see Figure 6).

In principle, if no ^{3}He is fed into the chamber, there is no source of nuclei able to induce CF_4 ionization/excitation. Nevertheless, due to the non-negligible Compton and photoelectric cross sections of gamma-rays in CF_4, the main contribution to the background spectrum is expected to have origin in this interaction. Figure 25 shows the $\text{QDC}_{\text{group}}$ counting rate distribution, measured after feeding the gas chamber with CF_4 at different pressures but; no ^{3}He. The decrease of the counting rate, in the region of the low charge, is linked to the P_{CF_4} reduction. It reflects the fact that background events are mainly produced by gamma-rays interacting with the CF_4 gas.

Most of the background gamma-rays at PSI are generated from two kinds of sources. First, from the de-excitation of nuclei product of the spallation process (proton on Pb/Zr), that can give place to gamma-rays of up to several MeV, and secondly, from de-excitation of neutron activated nuclei. Meanwhile the former occurs far from the delivery room, at the spallation target, the latter can be produced even by the materials constituting the detector. To evaluate the relative contribution of each source, future tests should include a detector gamma-shield.

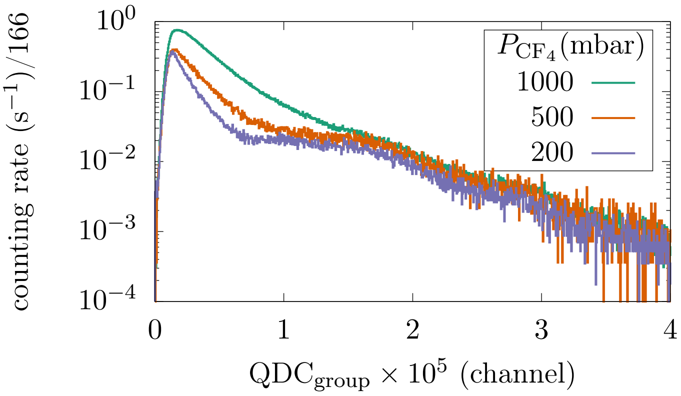

P_{CF_4} (mbar)	Total counting rate (s^{-1})
1000	67(8)
500	30(5)
200	20(4)

Figure 25 – Background charge spectra at PSI. Gas chamber filled with CF_4 at different pressures (P_{CF_4}) but no ^{3}He. In addition, the UCN entrance valve was closed. In general, the lower the pressure the lower the counting rate (total values in table below).

To establish how significant background counts are, events recorded with different operating conditions are compared against a normal UCN spectrum. In Figure 26, three types of background are displayed (labels b, c and d). The "beam" variable indicates whether the proton accelerator was working or not. No UCN are produced if the beam is switched off. Evidence of this is the spectrum label c; it is the only one that does not show the peak at charges close to channel 1.8×10^5. Background with label b is the same as the one with highest pressure already introduced in Figure 25. As for the special case in where the gas chamber is vacuumed[†] and the valve is left open (label d), there is still a conclusive distribution, UCN and very low charge events can still be detected, with a shallow rate though. This last issue is yet to be studied, by now it is attributed to gas residuals inside the chamber, and Cherenkov radiation from gamma-rays interacting with electrons in the output quartz windows.

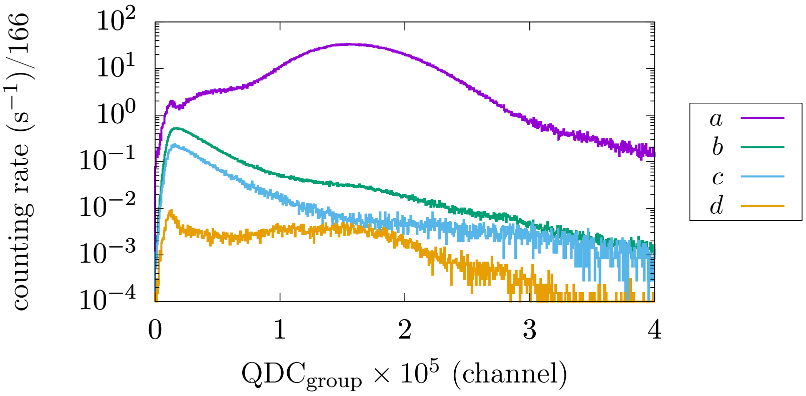

label	valve	beam	gas	total counting rate (s^{-1})
a	open	on	CF_4 & ^{3}He	7288(85)
b	closed	on	CF_4 & ^{3}He	49(7)
c	open	off	CF_4 & ^{3}He	19(4)
d	open	on	none	4(2)

Figure 26 – Three types of background (b, c and d) and normal UCN (a) counting rate spectra. Except for d, gas chamber filled with CF_4 at 1000 bar and ^{3}He at 15 mbar. Total counting rate and operating conditions description are resumed in the table.

The overall counting rates reported in Figure 26 are obtained from runs lasting more than 2 hours, that is, more than 20 proton cycles. Indeed, due to the non-regularity of the UCN flux, these overall values should be understood as the average counting rate along one cycle. This is clearly seen in UCN spectra (label a), whereas in previous sections the counting rate at the beam

---

[†] The turbo-pump employed for such purpose reported a vacuum in the order of 10^{-7} mbar.

pulse peak was observed near 5×10^4 s^{-1}, here the average after one cycle is $\sim 7 \times 10^3$ s^{-1}. Then, taking as reference this last number, the background counting rates do not exceed 1%.

Up to this point, the status of the background estimation is the following: accidental counts of single events, originated from electric noise and gamma-rays interacting with the PM components, are reduced by the coincidence technique to less than 1% the total counts; in addition, the background measurements show that events originated from the interaction of gamma-ray with the CF_4 gas and the Quartz windows (among others), also account for less than 1% the total counts. Therefore, it is expected at the most 2% of background contribution. Far from having included all the sources of non-desired events, this last result does not finish the analysis.

As the reader might have noticed, none of the background spectra (b, c and d) in Figure 26 accounts completely for the very low charge peak seen in the UCN distribution (a) around $\text{QDC}_{\text{group}} = 0.1 \times 10^5$. This difference is immediately linked to the fact that UCN delivery also causes non-UCN events. A fraction of the neutrons that never reach the gaseous chamber but rather escape towards the experiment area induce activation in all the instruments around, which in turn produce extra gamma background (neutron-induced gamma background). As a result, the amplitude of the low charge peak increases in UCN spectra. Such a phenomenon indicates that if a more effective background discrimination technique wants to be incorporated, coincidence signals from normal UCN delivery need to be examined individually.

3.4 Pulse shape analysis

Several detectors have the advantage of producing pulse signals whose patterns are representative of the detected particle or the interaction mechanism. Even when two pulses happen to have very similar areas (QDC), their amplitudes and decay times might differ considerably. Such differences, if adequately managed, represent a means to discriminate background events. Customary acquisition systems perform a first discrimination phase by setting voltage and time thresholds, that are used to filter, in real-time, the pulses not meeting the criteria (see two-dimensional trigger in section 2.3.1). Usually, imposing too complex requirements during the signal processing stage becomes a challenging task if a high rate is expected. In those cases, storing meaningful and quick-access information from the waveforms turns out to be the appropriate solution.

The following discussion is oriented towards the identification of waveform parameters that would make possible the discernment between UCN and background events. To this end, the SAMPLER module of FASTER was employed to record voltage pulses under two operating conditions, open and closed valve, both during regular proton cycles (beam on). Since it is not practical to show 10^6 waveforms in one plot, one might try to calculate the average pulse for both runs. However, by doing so, different events from the same run are mixed and no discrimination could be achieved. Instead, before performing any average, it is more convenient to extract the waveform parameters and then to evaluate any correlation among them.

In principle, multiple features of a waveform can be looked at so to define an accurate pulse shape discrimination process, it is also important to keep algorithms as simple as possible though. As a first stage, the current work proposes a discrimination approach based on the examination of two parameters, namely the grouped amplitude ($\mathrm{Amp}_{\mathrm{group}}$) and the integrated charge ($\mathrm{QDC}_{\mathrm{group}}$). To better understand its functioning, the following steps resume the algorithmic sequence:

1. Coincidence events are extracted from SAMPLER data. Let us suppose N coincidence groups.

2. The maximum amplitude ($\mathrm{Amp}_{\mathrm{PM}i}$) and integrated charge ($\mathrm{QDC}_{\mathrm{PM}i}$) are computed for the $3N$ waveforms (N for each PM).

3. Grouped values are calculated with equation 25 and

$$\mathrm{Amp}_{\mathrm{group}} = \sum_{i=1}^{3} \mathrm{Amp}_{\mathrm{PM}i} \tag{26}$$

4. Grouped charge-to-amplitude ratios are defined and calculated as

$$(\mathrm{QDC}/\mathrm{Amp})_{\mathrm{group}} = \mathrm{Amp}_{\mathrm{group}}/\mathrm{QDC}_{\mathrm{group}}. \tag{27}$$

5. Bidimensional histograms (correlation maps) are constructed with $\mathrm{Amp}_{\mathrm{group}}$ and $(\mathrm{QDC}/\mathrm{Amp})_{\mathrm{group}}$.

6. If different regions are evident from the map, cuts[‡] are defined and used to label the events in each region.

[‡] Data in this work is managed with ROOT TTrees structures, which allows the use of TCutG objects to separate events from correlation maps.

7. Average pulses are calculated from the events inside each region.
8. QDC$_{\text{group}}$ spectra are constructed showing the contribution of each region.

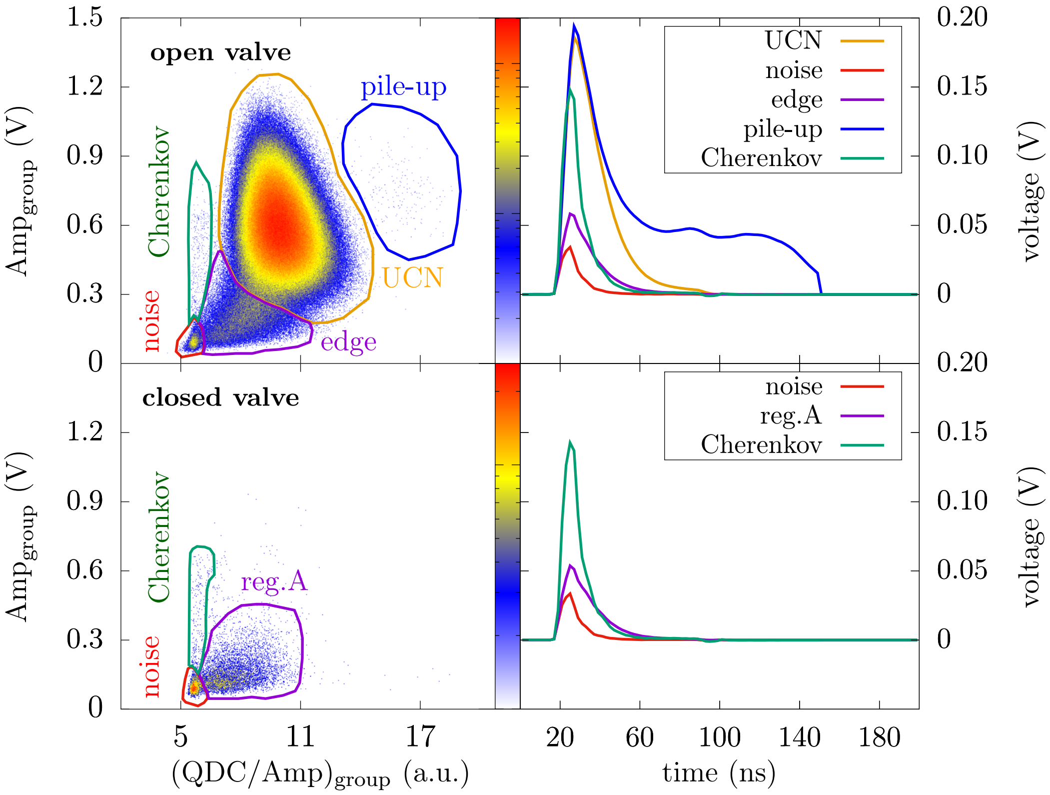

Region	decay time (ns)	
	open valve	closed valve
UCN	11.8(1)	-
noise	6.1(2)	6.0(1)
edge	12.1(3)	-
Cherenkov	7.7(2)	7.7(1)
reg.A	-	12.3(3)

Figure 27 – Pulse shape discrimination from amplitude vs. charge-to-amplitude ratio maps (left). Average pulse shape of events marked by the regions (right). Decay times obtained from fitting the average pulses are resumed in the table (bottom). The upper and lower plots correspond to data collected with open and closed valve, respectively. Whereas the 'UCN' region is completely absent for the latter, the 'edge' region overlaps with 'reg.A'. The color bar, with a logarithmic scale, indicates the number of events.

Figure 27 shows the result of steps 1 to 7 applied to the SAMPLER data collected with open (top) and closed (bottom) valve. The plots on the left correspond to the correlation maps, while the ones on the right to the average pulses. From a general viewpoint, the maps allow the identification of several regions that are characterized with distinct pulse shapes. The main difference is that, as expected, the 'UCN' spot is only seen when the valve is open.

Several facts can be pointed out from the correlation maps and the average pulses. However, in order to provide a more organized description, the analysis is articulated along with the result of last step in the discrimination algorithm, this is the charge spectra. Figure 28 depicts the charge distributions obtained from both runs; it is included as well the contribution of each region identified within the correlation maps.

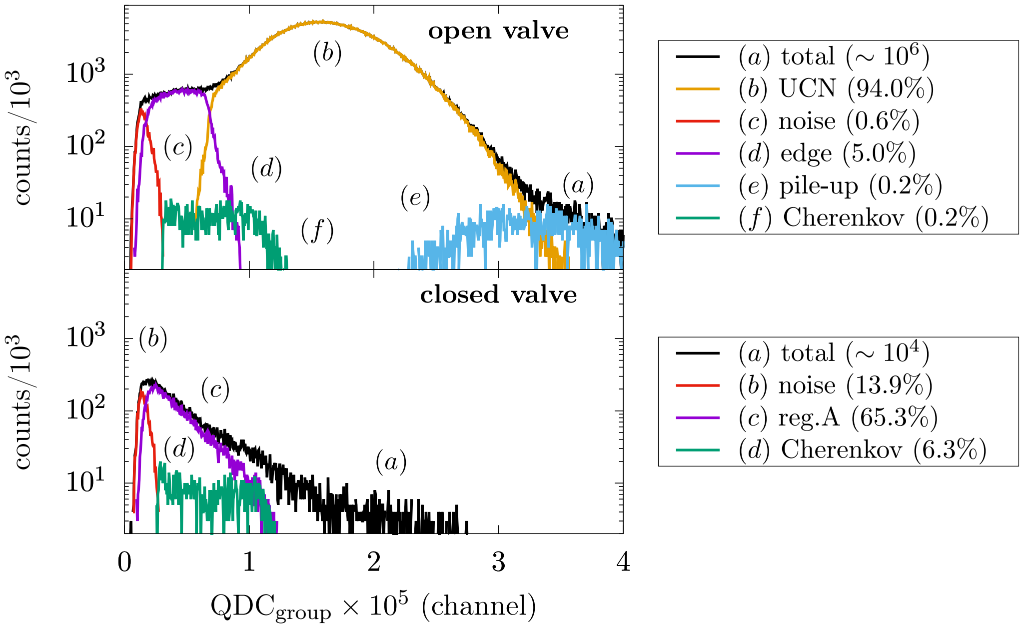

Figure 28 – Grouped charge spectrum for open and closed valve runs. Individual contributions from the regions defined in the correlation maps of Figure 27 are included.

Now that all the possible representations of the data are available, let us proceed with a brief discussion of the events inside each region:

- **UCN:** In 'open valve' conditions they correspond to the pulses with the highest amplitudes and longest decaying times. At the same time, the charge spectrum reveals that these events build the central peak up (therefore the name), with the largest overall contribution (94%).

On the other hand, in ‘closed valve’ conditions, there is no significant evidence of events inside this region.

- **pile-up:** Similarly as for ‘UCN’, these events are only seen when the valve is open. The center of its charge distribution is about two times the center of UCN, which suggests that this region corresponds to double UCN detection. This is confirmed with the ‘UCN’ rate ($\sim 2 \times 10^4$ s^{-1}) and the coincidence time window (2×10^{-7} s^{-1}); the pile-up rate with these conditions is about 78 s^{-1}, meaning a 0.3% of the total counts. Not included here, individual pulses show an evident double peak waveform.

- **Cherenkov:** Present in both operating conditions with similar absolute contributions, these events are not attributed to UCN interaction. The average pulse shape indicates that they have a large amplitude and fast decay time. Therefore, they should not be due to CF_4 scintillation but to a faster process. Among other sources of light inside the chamber, quartz windows are the most probable candidates. Gamma-rays interact with the electrons in the quartz that in turn, emit Cherenkov radiation [39]. This radiation process is characterized by a fast light emission, which fits with the observed from the average pulse.

- **noise:** These events show the shortest charges and amplitudes. The decay time is too short to be related to the CF_4 scintillation. From the correlation maps, it is appreciated that they are contained in a small region with a well defined local maximum. Thus, separation from UCN is straightforward. All these facts indicate that they correspond to accidental coincidences of electric noise.

- **reg.A:** Because UCN are not evidenced at all when the valve is closed, this region cannot have origin on them. Instead, based on their contribution to the charge spectrum and Figure 25, they are ascribed to the interaction of gamma-rays with the CF_4 gas. They represent the majority of events in ‘close valve’ conditions.

- **edge:** When looking at the correlation map, this region shows a uniform connection with the ‘UCN’ one. This constitutes the proof that edge events are included within the region. However, since ‘reg.A’ spans over a similar range with equal average pulses, gamma events might also be present. Due to such overlapping, the current discrimination approach is said to be limited to distinguish between gamma-rays interaction and edge events.

To summarize, pulse shape analysis based on amplitude and charge discrimination, following the eight-steps sequence previously outlined, allows the clear identification of three types of background events, labeled as ‘Cherenkov’, ‘pile-up’ and ‘noise’. The joint contribution of these events goes up to 1% of the total number of counts. The same algorithm also facilitates the ‘UCN’ discrimination, which yields a clean counting corresponding to 95%. Also, it has been proved that the remaining 5% is composed of edge and gamma events, with a relative contribution still not determined.

3.5 Efficiency as function of CF_4 and ^{3}He gases pressure

In the following, the spotlight will be put on the two main parameters that shape the detection efficiency of GADGET; they are the CF_4 and ^{3}He pressures. Two types of measurements were taken at the PSI UCN source to support this study. In both of them, one gas pressure was shifted while the other kept constant. This separated approach will be useful not only to suggest the optimal conditions but also to give an insight into the interaction process of UCN with the detector sensitive volume.

From previous analyses, it is possible to argue that $\sim$ 99% of the coincidence events corresponds to UCN interaction. Therefore, it is valid to attribute variations in the charge spectra to this kind. Besides, since the major changes occur in $\text{QDC}_{\text{group}}$ ranges at which only UCN are observed, background effects can safely be neglected.

To reduce the sources of systematic uncertainties, all the runs included in this section were recorded with similar conditions. On the one side, regarding the FASTER processing parameters, charge integration was calculated in a time window starting with the pulse trigger and lasting 150 ns, the validation gate for coincidence events was made 200 ns long, and the voltage and time thresholds for the three PMs were set in 3 mV and 2 ns, respectively. On the other side, data were extracted from the same time interval concerning the proton cycle, starting with the proton beam kick and finishing 25 s later. Such a period was enough to count more than 10^6 events, i.e., counting uncertainties reduced below 0.1%. However, since the total number of UCN delivered during this interval might no be equal far all the cycles, the GADGET counts (C_G) are normalized with the monitor counts (C_m), discussed in section 3.1.

3.5.1 Charge spectra dependency

One case of analysis is the CF_4 dependency. Figure 29 shows the charge spectra obtained with CF_4 at pressures ranging from 200 mbar to 1 bar, and ^{3}He at 15 mbar. The first and most evident feature is the reduction of the edge events at high pressures (contained between channels 0.1×10^5 and 1×10^5). This behavior agrees with the expected one since low P_{CF_4} implies long ionizing tracks, which in turn means high escape probability. In fact, the drastic change between 200 mbar and 400 mbar spectra, reflects the notable variance of the *ranges* (R) already reported in Figure 13. Another clear mark is the raise of the full-energy peak when P_{CF_4} increases. This comes from the fact that some of the events populating the 'edge' region at low pressures convert into full-energy deposition events at large ones. A first prediction would be a constant total number of counts, including all types of events, however it happens that this total reduces as the pressure grows. Such phenomenon is thoroughly reviewed in the next section.

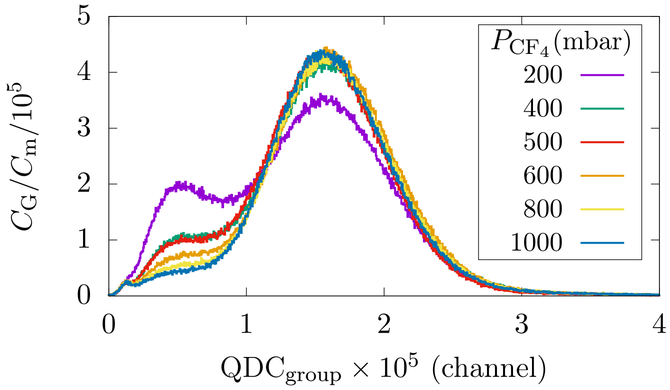

Figure 29 – Coincidence charge spectra at different CF_4 pressures. GADGET counts C_G are normalized with monitor counts C_m. The number of edge events (left bump) become less as the pressure increases. Some of those counts are recovered by the UCN peak, whose centroid remains constant. ^{3}He pressure was kept constant at 15 mbar.

Figure 29 also exhibits a not predicted result. This is the invariability of the UCN peak centroid, regardless of the CF_4 pressure, it is always found at charges close to 1.6×10^5. Contrary to what the alpha-irradiation study (Figure 12) could have suggested, this result is an indication of a constant photon yield in the range of pressures currently considered; it might happen that the light scintillation efficiency is different for alpha and proton or tritium irradiation. Finally, on the extremely low charges and slightly less visible, it also appears the 'noise' region. Its distribution, with charges $\lesssim 0.1 \times 10^5$, keeps a similar shape for all the spectra.

The second type of measurement is carried out by shifting the ^{3}He pressure ($P_{^3\text{He}}$). Figure 30 illustrates the spectra distribution obtained from runs with $P_{^3\text{He}}$ going from 5 mbar to 50 mbar, and P_{CF_4} fixed at 1 bar. Once again, there are cases where edge events are more likely. Here, the larger the pressure the greater the 'edge' region; when the helium pressure is augmented, the mean distance between the UCN absorption and the entrance wall is shortened, then enhancing the probability of tritium and proton escape. Opposite of what happens with CF_4, there is a significant difference between the areas of spectra at 5 mbar and 50 mbar. Given that the total number of counts is larger for the later, this behavior indicates that 5 mbar is not enough to stop all the UCN impinging the gas chamber, some of them find their way out after crossing it.

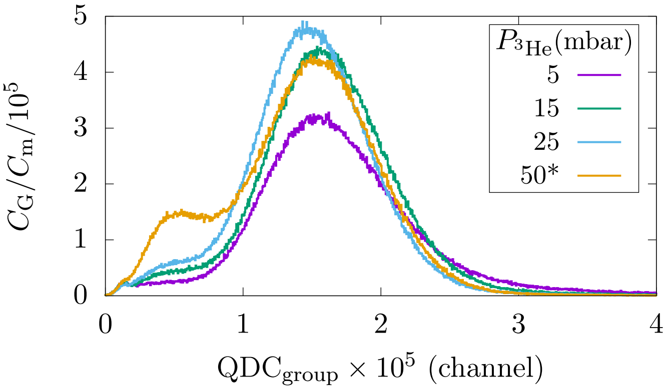

Figure 30 – Coincidence charge spectra at different ^{3}He pressures. GADGET counts C_G are normalized with monitor counts C_m. The number of edge events (left bump) grows as the pressure increases. CF_4 pressure was kept constant at 1 bar. The asterisk is used to indicate the insertion of an extra variable in the 50 mbar run (the ^{3}He for this run was supplied from a different source).

3.5.2 Overall counting rate study

Because both edge and full-energy events have origin in UCN absorption, their joint contribution is indicative of the total UCN detection. Analyses in the previous section suggested that the gas pressures affect the total number of UCN counts. However, before reporting any value, let us set out a brief description of the interaction of UCN with the gas mixture of GADGET.

Two mechanisms determine the behavior of UCN when they enter the gas chamber. They are the absorption and upscattering from both ^{3}He and CF_4. Here, upscattering refers to the non-elastic scattering process that makes UCN disperse while gaining kinetic energy from the collided nucleus at thermal energies. When UCN undergo upscattering, their energies increase to a level at which the gases and chamber become transparent (they are not longer ultracold), enabling them to go across the detector without being absorbed.

One way to estimate the relative amount of UCN absorbed and upscattered by the gases, is through the *mean free path*. It is calculated as

$$\lambda = (\Sigma_m)^{-1} = \left(\sum n_i \sigma_i\right)^{-1}, \tag{28}$$

in where Σ_m stands for the macroscopic cross section, which accounts for all the possible interaction mechanisms with microscopic cross section σ_i. In particular, for the processes involved in the chamber, it is written as

$$\Sigma_m = (n\sigma_{\text{up}})_{\text{CF}_4} + (n\sigma_{\text{ab}})_{\text{CF}_4} + (n\sigma_{\text{up}})_{^3\text{He}} + (n\sigma_{\text{ab}})_{^3\text{He}}, \tag{29}$$

in where σ_{ab} and σ_{up} represent the absorption and upscattering cross sections, respectively. This last expression depends not only on the individual cross sections (whose magnitudes are resumed in Table 3), but also on the gas densities n_{CF_4} and $n_{^3\text{He}}$. For the operating conditions considered so far, it happens that

$$\frac{n_{^3\text{He}}}{n_{\text{CF}_4}} = \frac{P_{^3\text{He}}}{P_{\text{CF}_4}} \approx 10^{-2}. \tag{30}$$

Thus, looking at the products $n_i\sigma_i$, it results that out of the four terms in the macroscopic cross section, two of them are the most significant ones

$$\begin{aligned}
\Sigma_m \approx& (n\sigma_{\text{up}})_{\text{CF}_4} + (n\sigma_{\text{ab}})_{^3\text{He}} && (31)\\
=& n_{\text{up}}\sigma_{\text{up}} + n_{\text{ab}}\sigma_{\text{ab}} && (32)\\
=& \frac{1}{K_B T}\left(P_{\text{CF}_4}\sigma_{\text{up}} + P_{^3\text{He}}\sigma_{\text{ab}}\right), && (33)
\end{aligned}$$

in where the *ideal gas law* has been used to express the densities as function of the pressures; also it is adopted the convention that the subscript "up" refers only to CF_4 and "ab" to ^{3}He.

In conclusion, the UCN *mean free path* is governed by the upscattering of CF_4 and the absorption of ^{3}He. Starting from this premise and assuming an

Table 3 – Cross sections of gases used in GADGET detector. σ_{up} for CF$_4$ reported by Seestrom *et al* [40]. Other values have been escaled from NIST database to UCN velocity 6.6 m/s.

	σ_{ab} (barn)	σ_{up} (barn)
^{3}He	1 777 667(2333)	2 000(133)
CF$_4$	14	3 300(660)

ideal scenario in where UCN enter normally into the gas chamber, the total absorption probability is calculated as (see the deduction in Appendix A)

$$\mathcal{P}_{\mathrm{ab}}^{\mathrm{tot}}(P_{^3\mathrm{He}}, P_{\mathrm{CF}_4}) = \frac{P_{^3\mathrm{He}}\sigma_{\mathrm{ab}}}{P_{\mathrm{CF}_4}\sigma_{\mathrm{up}} + P_{^3\mathrm{He}}\sigma_{\mathrm{ab}}} \left[1 - \exp\left(-L/\lambda\right)\right], \tag{34}$$

with L the length of the gas chamber. This equation shows that while large CF$_4$ pressures attenuate the absorption, large ^{3}He pressures enhance it. At this point it results suitable to report the counting rates (r) calculated from the integrals of spectra in Figures 29 and 30. With the purpose of comparing them against the model in equation 34, Figure 31 shows the trends of $r(P_{^3\mathrm{He}}, P_{\mathrm{CF}_4})$ and $\mathcal{P}_{\mathrm{ab}}^{\mathrm{tot}}(P_{^3\mathrm{He}}, P_{\mathrm{CF}_4})$ in the two situations $P_{^3\mathrm{He}}$ (bottom) and P_{CF_4} (top) variation, whose displayed values are normalized to $P_{^3\mathrm{He}} = 15$ mbar and $P_{\mathrm{CF}_4} = 200$ mbar, respectively.

The counting rate trends observed in Figure 31 agree to a large extent with the ones predicted from the analytical model. These plots allow the formulation of two quantitative assertions. First, about 7% of the counts are profited when decreasing P_{CF_4} from 1000 mbar to 200 mbar. This improvement added to the fact that gamma-ray background is proportional to the CF$_4$ gas density, suggests working with low P_{CF_4}. Second, raising the helium pressure from 10 to 15 mbar represents an extra 5% gain. In the end, the overall effect of both changes would signify an enhancement of 10% of the counts. That being said, two liming cases should be avoided, they are too low P_{CF_4} and too large $P_{^3\mathrm{He}}$. The predominance of edge events in such cases makes the gamma events difficult to identify.

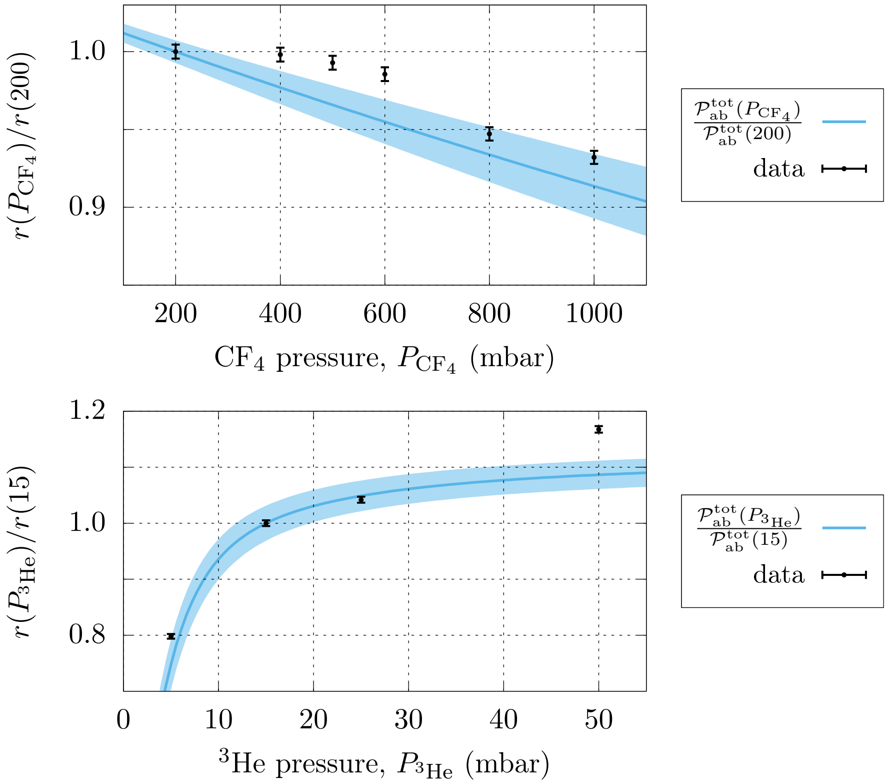

Figure 31 – Measured counting rate as a function of the ^{3}He pressure with respect to 15 mbar result (bottom), and as a function of the CF$_4$ pressure with respect to 200 mbar result (top). The solid lines correspond to the absorption probability as determined by equation 34. The thickness of the lines represents the uncertainty propagated from σ_{ab} and σ_{up}.

4 Performance at Mainz's TRIGA reactor

The second test, this time with the UCN source from the TRIGA reactor at the Nuclear Chemistry department of the Johannes Gutenberg University in Mainz, had as a purpose that of carrying out an absolute comparison between the UCN counting rates achieved by the GADGET and cascade-type detectors. Regarding the GADGET and FASTER inner parameters, data was collected under similar conditions as in PSI. Both detectors were located at the same point of the UCN delivery guide, one after the other. No monitor detector was used since the UCN delivery was always operated in constant mode. The experimental setup has not many more details apart from those already illustrated in Figure 7.

4.1 Background estimation

Background radiation close to nuclear reactors is entirely different from the one near particle accelerators. Product of the fission processes, gamma-ray emissions in reactors are considerably more abundant than the ones observed in accelerator facilities; even in sub-critical mode (shut-down), fission still occurs at the reactor core. This, added to the large variety of isotopes created from uranium fission, implies a background broader in range and amplitude.

Evidence of the non-negligible contribution of background events to the UCN counting rate with GADGET is shown in Figure 32. Similarly as in PSI, the background measurement is estimated in two cases, one after closing the UCN delivery valve, and the other when the reactor is shut-down. The total counting rates, obtained from the areas, indicate that 'closed valve' background events account for $\sim 37\%$ of the UCN counting, and 'reactor off' only for a 0.2%. It is not only remarkable the magnitude of the former but also its charge distribution. It shows that apart from gamma-rays, neutrons also make part of the background (bump near $\mathrm{QDC}_{\mathrm{group}} = 1.6 \times 10^5$ in spectra *b*). This extra contribution is attainted to the fast neutrons that exit the reactor walls and scatter in the experiment hall towards the detector. Even if they have thermal energies, there is a certain probability of being absorbed by the ^{3}He gas.

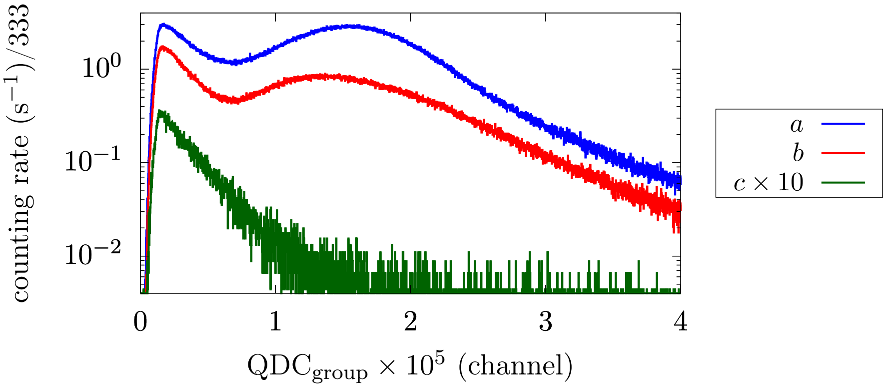

label	valve	reactor	total counting rate (s^{-1})
a	open	on	2960(54)
b	closed	on	1097(33)
c	open	off	7(3)

Figure 32 – Counting rate charge spectra at TRIGA (top). UCN and two types of background are displayed. The integrated counting rates and operating conditions are resumed in the table. CF_4 filled at 1 bar and ^3He at 15 mbar.

The first and most straightforward way to calculate the actual UCN counts is by subtracting the 'closed' from the 'open' rate. However, as shown by the white-blue spectra on the right side of Figure 33, gamma-rays counts are still notable in the low charges range after the subtraction. This *simple* approach lacks accuracy due to the underestimation of the gamma-rays produced from neutron activation. When the valve is open, there are more neutrons available to induce such a process.

A second phase in the background subtraction corrects the missed gamma-rays events. It uses the 'closed valve' distribution to predict a γ-shape that later is recalibrated and subtracted from the spectrum resulting in the first subtraction. The implementation of the proposed method is resumed by the following steps

1. An overall fit is performed to the 'closed valve' spectrum. The fitting function is composed of an exponential (γ-fit), and two Gaussians (peak 1 and 2). The left side of Figure 33 works as an example.

2. The γ-fit function is recalibrated to the 'open minus closed valve' spectrum. In this new adjustment, just the amplitude is changed; the decay

constant is kept fixed. The fitting range is chosen appropriately so to cover the gamma range only.

3. The new γ-fit function is subtracted from the 'open minus closed valve' spectrum.

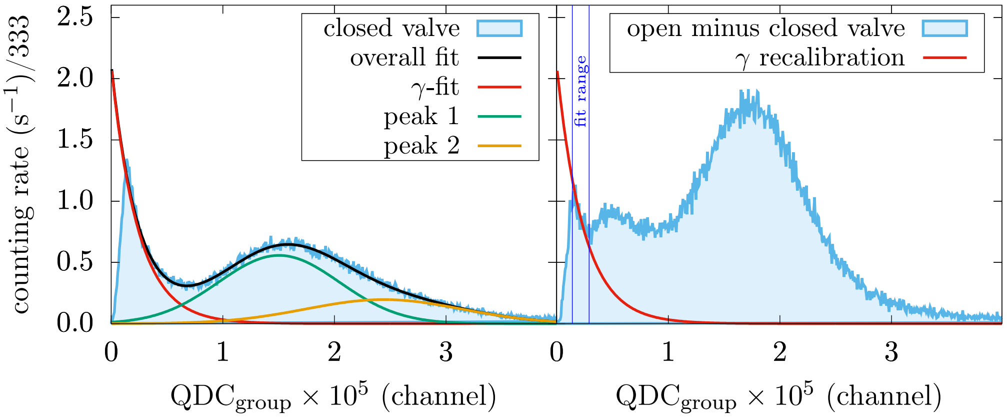

Figure 33 – Representation of the second phase in the background subtraction. A first γ-fit is extracted from the 'closed valve' spectrum (left), that consequently is recalibrated and subtracted from the 'open minus closed valve' spectrum (right).

The prescribed method is applied to three runs at a different CF_4 pressures. The spectra resulting from the first (simple) and second (double) phases of the background subtraction are illustrated in Figure 34. After looking both cases, it appears evident how the 'double' subtraction process allows the identification of the edge region, that was hidden in the 'simple' version. Once again, it is observed the decrease of edge events at large CF_4 pressures. The reproduction of this tendency is used to validate the current method of background subtraction.

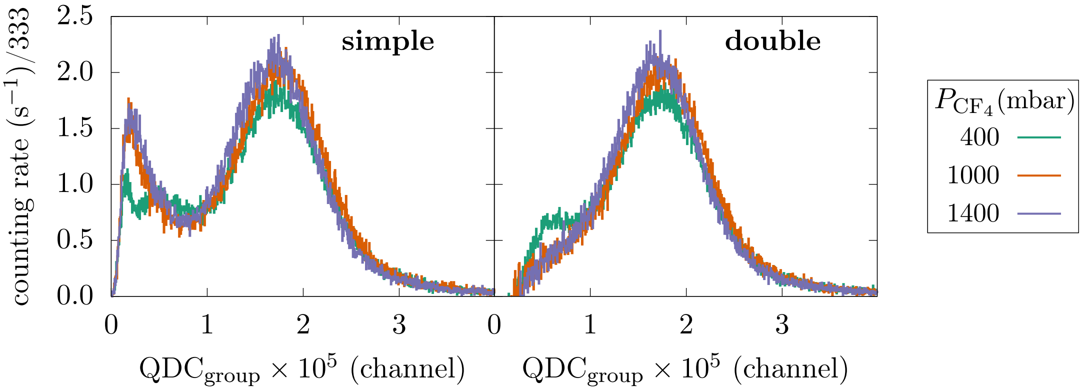

Figure 34 – Spectra resulting from the first (simple) and second (double) phases of the background subtraction method. Three different CF_4 pressures are studied. The double subtraction reveals the edge events region.

4.2 Counting rate comparison

The total UCN counting rates achieved with GADGET (r_G) are compared against the one measured with a cascade-type detector (r_{cascade}). Because both apparatuses count with entrance windows of equal sizes, it is reasonable to confront their efficiencies to count UCN at the end of the same delivery guide. Based on the results of the tests at PSI, the operating conditions for GADGET were chosen in such a way that its maximum (or close to the maximum) efficiency could be exploited. While ^{3}He pressure was fixed at 25 mbar, three different CF_4 pressures were tested. As for the background, it was estimated and reduced through the method discussed in the previous section.

Table 4 – Counting rates measured with GADGET (r_G) and their relative differences with respect to the one measured with cascade detector ($r_{\text{cascade}} = 785(28)\ \text{s}^{-1}$). 'simple' and 'double' columns represent the two kind of background subtraction presented in section 4.1.

P_{CF_4} (mbar)	r_G (s^{-1}) simple	r_G (s^{-1}) double	$\frac{r_{\text{cascade}}}{r_{\text{G-double}}} \times 100$ (%)
400	1631(40)	1443(38)	54(2)
1000	1787(42)	1478(38)	53(2)
1400	1818(43)	1407(37)	56(2)

Table 4 resumes the counting rates calculated with GADGET, and the difference they represent against the cascade performance ($r_{\text{cascade}} = 784(28)$

s^{-1}). Background counts have already been subtracted from the reported values; both 'simple' and 'double' background estimations have been considered for r_G. The evidence suggests that GADGET detects slightly more than twice the number detected by the cascade-type. Since spectroscopy analysis is not possible in the cascade detector, its background estimation is obtained from the 'closed valve' configuration ('simple' estimation). Therefore, its actual performance could be inferior to the stated before.

Among the possible factors raising the difference between r_G and r_{cascade}, the entrance foil plays a significant role. The same cascade detector has been tested before with other foil materials. It was reported [41] that a 25% could be gained if the cascade is operated with a 100 μm $AlMg_3$ foil (instead of the current one). A second reason for the UCN counting defect in the cascade-type is the complete absorption by its boron layer, whose thickness is of a few μm. When the reaction products are expelled along the plane defined by the layer, they cannot reach the ionization chamber and consequently are missed[§][25]. The contribution of such effect has been estimated around 15%, thus, taking into account the 10% variation between foils of 100 μm and 30 μm (see Table 2), the total fraction of UCN lost in this detector is

$$\delta_{\text{tot}} \approx 25\% + 15\% + 10\% = 50\% \tag{35}$$

which agrees with the values reported in Table 4.

[§] This issue does not exist for the GADGET detector given that its sensitive volume is in a gaseous state.

5 Conclusions and perspectives

The novel UCN gaseous detector, based on the neutron absorption of ^{3}He and on the scintillation of CF_4, was introduced as an alternative to the already existing detection systems. GADGET capabilities were tested with UCN provided by two facilities, the PSI and the Mainz TRIGA reactor sources. The former made possible the characterization of the processes triggered by the UCN absorption inside GADGET's gas chamber, and the latter was used to evaluate its UCN counting efficiency.

Data acquisition was completed with FASTER modules which, allowed the digital recording of voltage waveforms with sampling times of 2 ns. From data collected at PSI, the background contribution to the UCN counting was estimated at $\sim 2\%$. The origin of such events was explored through pulse shape analysis based on the amplitude and integrated charge. The majority of the background events are attributed to gamma-rays interacting with the CF_4 gas. Cherenkov radiation, electric noise, and pile-up events were also evidenced, but with a less significant contribution ($\lesssim 1\%$ all of them together). There is still a need to improve the discrimination between gamma and edge events though.

The optimal operating conditions for GADGET were found at gas pressures of around 400 mbar for CF_4 and 25 mbar for ^{3}He. Larger CF_4 pressures increase the probability of UCN upscattering and gamma-ray interaction, while shorter ones imply more edge events. Conversely, whereas higher ^{3}He pressures produce significant amounts of edge events, shorter ones signify several UCN crossing the gas chamber without being absorbed.

Roughly speaking, GADGET resulted doubly more efficient than the ^{10}B-based cascade detector. Although this difference is highly dependent on the entrance foil features, the design of GADGET enables the use of thinner foils. In addition, features such as the ability to reduce UCN losses, high rate capability, inclusion of the pulse shape discrimination phase, and the versatility regarding the gases and light collectors convert GADGET in one of the best candidates for the UCN counting in the n2EDM experiment.

A Absorption probability

UCN traveling in a gaseous mixture composed of CF_4 and ^{3}He can undergo upscattering and absorption from either gas. However, out of the four processes, only the absorption of ^{3}He and the upscattering of CF_4 are significant.

The following procedure allows estimating the overall absorption probability for UCN impinging normally ($\hat{x}$) on a gas chamber with length L.

On the one hand, as in any process in where a *mean free path* can be defined, the probability for UCN not to interact (survival probability) after crossing a distance x inside the gas is

$$\mathcal{P}_{\text{sur}}(x) = \exp\left(-x/\lambda\right), \tag{36}$$

with λ the *mean free path*, calculated as

$$\lambda = \frac{1}{\Sigma_i n_i \sigma_i} = \frac{1}{n_{\text{up}}\sigma_{\text{up}} + n_{\text{ab}}\sigma_{\text{ab}}} \tag{37}$$

in where n_{ab} and n_{up} are the densities of nuclei producing the absorption (^{3}He) and upscattering (CF_4), and σ_{ab} and σ_{up} their corresponding cross sections (Figure 35 shows the behavior of λ as function of the gases pressures).

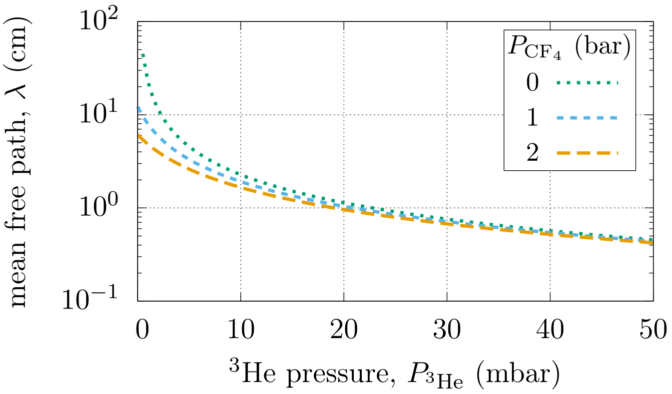

Figure 35 – UCN *mean free path* in gas mixture ^{3}He-CF_4 at different pressures.

On the other hand, the UCN absorption probability in an infinitesimal layer of thickness dx is given by

$$\mathcal{P}_{\text{ab}} = n_{\text{ab}}\sigma_{\text{ab}}dx. \tag{38}$$

Then, the probability for absorption between x and $x + dx$, once the UCN has reached x, is

$$\begin{aligned} \mathcal{P}_{\mathrm{ab}}(x) &= \mathcal{P}_{\mathrm{sur}}(x) \cdot \mathcal{P}_{\mathrm{ab}} \qquad (39) \\ &= \exp\left(-x/\lambda\right) \cdot \left(n_{\mathrm{ab}}\sigma_{\mathrm{ab}}dx\right), \qquad (40) \end{aligned}$$

whose integral, between $x = 0$ and $x = L$, represents the total absorption probability in the chamber:

$$\begin{aligned} \mathcal{P}_{\mathrm{ab}}^{\mathrm{tot}} &= \int_0^L \exp\left(-x/\lambda\right) n_{\mathrm{ab}}\sigma_{\mathrm{ab}}dx \qquad (41) \\ &= n_{\mathrm{ab}}\sigma_{\mathrm{ab}}\lambda[1 - \exp\left(-L/\lambda\right)] \qquad (42) \\ &= \frac{n_{\mathrm{ab}}\sigma_{\mathrm{ab}}}{n_{\mathrm{up}}\sigma_{\mathrm{up}} + n_{\mathrm{ab}}\sigma_{\mathrm{ab}}}[1 - \exp\left(-L/\lambda\right)]. \qquad (43) \end{aligned}$$

References

[1] Khriplovich, I. B., Lamoreaux, S. (1997). *Cp violation without strangeness: Electric dipole moments of particles, atoms, and molecules*. Springer-Verlag Berlin Heidelberg. 10.1007/978-3-642-60838-4

[2] Smith, J. H., Purcell, E. M., & Ramsey, N. F. (1957). *Experimental Limit to the Electric Dipole Moment of the Neutron*. Physical Review, 108(1), 120-122. doi:10.1103/physrev.108.120

[3] Lüders, G. (1957). *Proof of the TCP theorem*. Annals of Physics, 2(1), 1-15. doi: 10.1016/0003-4916(57)90032-5

[4] Dubbers, D., & Schmidt, M. G. (2011). *The neutron and its role in cosmology and particle physics*. Reviews of Modern Physics, 83(4), 1111-1171. doi:10.1103/revmodphys.83.1111

[5] Baker, C. A., *et al.* (2006). *Improved Experimental Limit on the Electric Dipole Moment of the Neutron*. Physical Review Letters, 97(13). doi:10.1103/physrevlett.97.131801

[6] Roberts, B. L., & Marciano, W. J. (2009). *Lepton dipole moments*. New Jersey: World Scientific Publishing Company. doi:https://doi.org/10.1142/7273

[7] Abel, C. *et al.* (2019). *The n2EDM experiment at the Paul Scherrer Institute*. arXiv:1811.02340

[8] Ramsey, N. F.,. (1950). *A Molecular Beam Resonance Method with Separated Oscillating Fields*. Physical Review, 78(6), 695-699. doi:10.1103/physrev.78.695

[9] Altarev, I., *et al.* (2009). *Towards a new measurement of the neutron electric dipole moment*. Nuclear Instruments and Methods in Physics Research Section A: Accelerators, Spectrometers, Detectors and Associated Equipment, 611(2-3), 133-136. doi:10.1016/j.nima.2009.07.046

[10] Rabi, I. I. (1937). *Space Quantization in a Gyrating Magnetic Field*. Physical Review, 51(8), 652-654. doi:10.1103/physrev.51.652

[11] Becker, H., *et al.* (2015). *Neutron production and thermal moderation at the PSI UCN source.* Nuclear Instruments and Methods in Physics Research Section A: Accelerators, Spectrometers, Detectors and Associated Equipment, 777, 20-27. doi:10.1016/j.nima.2014.12.091

[12] Heinz Maier-Leibnitz Zentrum. *UCN source - FRM II.* https://www.mlz-garching.de/ucn (viewed jul-2019).

[13] TRIUMF. *TRIUMF's Ultracold Neutron (UCN) facility.* https://www.triumf.ca/ucn (viewed jul-2019).

[14] Institut Laue–Langevin. *UCN Source SuperSUN.* https://www.ill.eu/users/support-labs-infrastructure/sample-environment/equipment/low-temperature/ucn-source-supersun/ (viewed jul-2019).

[15] Oak Ridge National Laboratory. *Spallation Neutron Source.* https://www.phy.ornl.gov/nedm/ (viewed jul-2019).

[16] Golub, R., Richardson, D., & Lamoreaux, S. K. (1991). *Ultra-cold neutrons.* Bristol: Adam Hilger.

[17] Paul Scherrer Institut. *The UCN facility.* https://www.psi.ch/en/bsq/ucn-facility (viewed jul-2019).

[18] Dyson, F. J. (2001). *Disturbing the universe.* New York: Basic Books.

[19] Frei, A.,*et al.* (2007). *First production of ultracold neutrons with a solid deuterium source at the pulsed reactor TRIGA Mainz**. The European Physical Journal A, 34(2), 119-127. doi:10.1140/epja/i2007-10494-2

[20] Karch, J.. (2014). *Performance of the solid deuterium ultra-cold neutron source at the pulsed reactor TRIGA Mainz.* The European Physical Journal A, 50(4). doi:10.1140/epja/i2014-14078-9

[21] Gwendal, R,. (2009). *Développement de détecteurs de neutrons ultra-froids et d'un système d'analyse de polarisation pour la mesure de l'EDM du neutron.* Diploma thesis.

[22] Knoll, G. F. (2010). *Radiation detection and measurement.* Hoboken, NJ.: John Wiley & Sons.

[23] Ban, G.,*et al.* (2016). *Ultracold neutron detection with ^{6}Li-doped glass scintillators*. The European Physical Journal A, 52(10). doi:10.1140/epja/i2016-16326-4

[24] Scintacor. *6-lithium glass*. https://scintacor.com/products/6-lithium-glass/ (viewed jul-2019).

[25] Klein, M., & Schmidt, C. J. (2011). *CASCADE, neutron detectors for highest count rates in combination with ASIC/FPGA based readout electronics*. Nuclear Instruments and Methods in Physics Research Section A: Accelerators, Spectrometers, Detectors and Associated Equipment, 628(1), 9-18. doi:10.1016/j.nima.2010.06.278

[26] Piegsa, F. M., *et al.* (2014). *New source for ultracold neutrons at the Institut Laue-Langevin*. Physical Review C, 90(1). doi:10.1103/physrevc.90.015501

[27] Imajo, S., *et al.* (2016). *Pulsed ultra-cold neutron production using a Doppler shifter at J-PARC*. Progress of Theoretical and Experimental Physics, 2016(1). doi:10.1093/ptep/ptv177

[28] Saunders, A. *et al.* (2004). *Demonstration of a solid deuterium source of ultra-cold neutrons*. Physics Letters B, 593(1-4), 55-60. doi:10.1016/j.physletb.2004.04.048

[29] Takahashi, T. *et al.* (1983). *Emission spectra from Ar-Xe, Ar-Kr, Ar-N_2, Ar-CH_4, Ar-CO_2 and Xe-N_2 gas scintillation proportional counters*. Nuclear Instruments and Methods in Physics Research, 205(3), 591-596. doi:10.1016/0167-5087(83)90028-5

[30] Lehaut, G. *et al.* (2015). *Scintillation properties of N_2 and CF_4 and performances of a scintillating ionization chamber*. Nuclear Instruments and Methods in Physics Research Section A: Accelerators, Spectrometers, Detectors and Associated Equipment, 797, 57-63. doi:10.1016/j.nima.2015.05.050

[31] Goupilliere, D. (2018). Private communication.

[32] Morozov, A. *et al.* (2011). *Effect of the electric field on the primary scintillation from CF_4*. Nuclear Instruments and Methods in Physics

Research Section A: Accelerators, Spectrometers, Detectors and Associated Equipment, 628(1), 360-363. doi:10.1016/j.nima.2010.07.001

[33] Morozov, A. *et al.* (2010). *Photon yield for ultraviolet and visible emission from CF4 excited with α-particles*. Nuclear Instruments and Methods in Physics Research Section B: Beam Interactions with Materials and Atoms, 268(9), 1456-1459. doi:10.1016/j.nimb.2010.01.012

[34] Ziegler, J. F., Ziegler, M., & Biersack, J. (2010). SRIM – *The stopping and range of ions in matter* . Nuclear Instruments and Methods in Physics Research Section B: Beam Interactions with Materials and Atoms, 268(11-12), 1818-1823. doi:10.1016/j.nimb.2010.02.091

[35] Hamamatsu. *Photomultiplier tubes R1828-01, R2059.* https://www.hamamatsu.com/eu/en/product/type/R2059/index.html (viewed jul-2019).

[36] Fast Acquisition System for nuclEar Research. *FASTER PROJECT*. http://faster.in2p3.fr/ (viewed jul-2019).

[37] Dechenaux, B. (2015). Private communication.

[38] Eckart, C., & Shonka, F. R. (1938). *Accidental Coincidences in Counter Circuits*. Physical Review, 53(9), 752-756. doi:10.1103/physrev.53.752

[39] Moore, A. S. *et al.* (2018). *A fused silica Cherenkov radiator for high precision time-of-flight measurement of DT γ and neutron spectra (invited).* Review of Scientific Instruments, 89(10). doi:10.1063/1.5039322

[40] Seestrom, *et al*, (2015). *Upscattering of ultracold neutrons from gases.* Physical Review C, 92(6). doi:10.1103/physrevc.92.065501

[41] Lauss, B. *et al.* (2019). Private communication.